


Mitigation of quantum crosstalk in cross-resonance-based qubit architectures

Peng Zhao^{1,2,*}

¹Tongling, Anhui 244000, China

²Beijing Academy of Quantum Information Sciences, Beijing 100193, China

 (Received 25 July 2023; revised 16 September 2023; accepted 1 November 2023; published 15 November 2023)

The cross-resonance gate (CR gate) architecture that exploits fixed-frequency transmon qubits and fixed couplings is a leading candidate for quantum computing. Nonetheless, without the tunability of qubit parameters such as qubit frequencies and couplings, gate operations can be limited by the presence of quantum crosstalk arising from the always-ON couplings. When increasing system sizes, this can become even more serious, considering frequency collisions caused by fabrication uncertainties. Here, we introduce a CR-gate-based transmon architecture with passive mitigation of both quantum crosstalk and frequency collisions. Assuming typical parameters, we show that ZZ crosstalk can be suppressed while maintaining XY couplings to support fast, high-fidelity CR gates. The architecture also allows one to go beyond the existing literature by extending the operating regions in which fast, high-fidelity CR gates are possible, thus alleviating the frequency-collision issue. To examine the practicality, we analyze the CR-gate performance in multiqubit lattices and provide an intuitive model for identifying and mitigating the dominant source of error. For the state-of-the-art precision in setting frequencies, we further investigate its impact on the gates. We find that ZZ crosstalk and frequency collisions can be largely mitigated for neighboring qubits, while interactions beyond near-neighbor qubits can introduce new frequency collisions. As the strength is typically at the submegahertz level, adding weak off-resonant drives to selectively shift qubits can mitigate the collisions. This work could be useful for suppressing quantum crosstalk and improving gate fidelities in large-scale quantum processors based on fixed-frequency qubits and fixed couplings.

DOI: [10.1103/PhysRevApplied.20.054033](https://doi.org/10.1103/PhysRevApplied.20.054033)

I. INTRODUCTION

Achieving high-fidelity qubit operations in scaling up qubit architectures is one of the most fundamental challenges in quantum computing [1]. With demonstrations of long coherence times, ease of control, and flexibility in design, superconducting qubits hold great promise for implementing large-scale quantum processors. Accordingly, diverse qubit architectures based on superconducting qubits have been developed during the past two decades [2,3]. However, until now, very few of those have demonstrated significant improvements in both system sizes and gate fidelities. Besides qubit decoherence, the main obstacle is due to the presence of quantum crosstalk arising from residual qubit-qubit couplings [4]. This highlights the importance of understanding the quantum crosstalk and figuring out how to address this issue for building large-scale superconducting quantum processors.

The cross-resonance gate (CR gate) is an all-microwave-controlled two-qubit gate for superconducting qubits,

which is implemented by driving the control qubit at the frequency of the target qubit [5–8], and has been shown to have considerable potential for building large-scale quantum processors based on transmon qubits [9]. For instance, the past decade has witnessed tremendous progress toward improving both the system size and gate performance for the CR-gate-based transmon architecture, which has led to the demonstrations of small-scale error-correction codes [10,11] and the exploration of quantum advantage before fault tolerance [12]. To be more specific, the system size can reach the 100-qubit level [12], and the typical single-qubit gate error is close to 10^{-4} while the two-qubit gate error is below 10^{-2} [10–13].

This progress mainly benefits from the appealing feature of the CR architecture, i.e., universal qubit operations are solely based on microwave drives [14]. Compared to qubit architectures with tunable elements [2,3], this feature supports the practical advantage offered by combining the long coherence time of nontunable elements such as single-junction transmons [15–17] and the low overhead of all-microwave control [2,14,18]. This eventually yields the most widely explored CR architecture

*shangniguo@sina.com

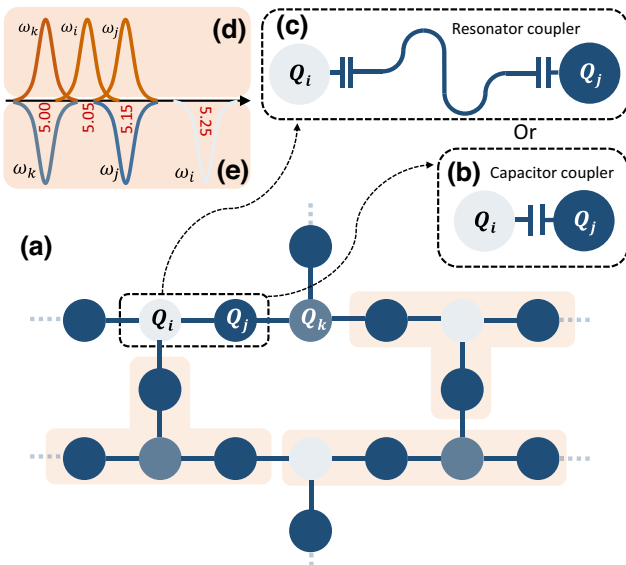


FIG. 1. (a) The heavy-hexagonal qubit lattice. The circles denote transmons while the edges represent couplers, which could be either a capacitor (b) or a resonator (c). Here, a three-frequency pattern indicated in three colors (dark blue, light gray, and dark gray) is employed to avoid frequency collisions. For CR architectures, the dark-blue circles denote the control qubits, e.g., Q_j with the typical frequency ω_j , and the light (dark) gray circles denote the target qubits, e.g., $Q_{i(k)}$ with the typical frequency $\omega_{i(k)}$. (d) Typical distributions of qubit frequencies in the existing literature, where, to ensure fast gates, the control qubit frequency is higher than the target qubit frequency ($\omega_j > \omega_i > \omega_k$), giving positive control-target detunings. (e) Typical frequency allocation for the proposed architecture, where qubits are coupled via a resonator, as in (b), and the three distinct frequencies satisfy the condition $\omega_i > \omega_j > \omega_k$, allowing for further mitigating frequency collisions. This is enabled by an appealing feature of the proposed architecture, e.g., even under conditions of negative control-target detunings, high-fidelity CR gates can still be achieved with gate speeds comparable to those with positive detunings.

wherein fixed-frequency transmons are fixedly coupled via a coupling capacitor [19,20] or a bus resonator [14,21], as shown in Fig. 1. However, as one might expect, there is no such thing as a free lunch: the lack of frequency-tunable elements also means that, unlike qubit architectures with tunable elements, generally, there is no active approach available for mitigating undesirable effects, such as qubit frequency collisions owing to the inaccuracy in setting qubit frequencies [22–25] and quantum crosstalk arising from residual couplings and the weak anharmonicity of transmons [18,26–31]. To this end, within the CR architecture, one has to devise passive approaches to addressing these challenges.

For the CR architecture, quantum crosstalk can be manifested in many forms, such as ZZ crosstalk [18,26–28], next-neighboring interactions [29–31], and undesirable

multiphoton transitions [29,31]. More importantly, it can become even more serious when qubit frequency collisions happen [29–31]. To alleviate such concerns, considerable efforts have been made, such as improving the accuracy in setting qubit frequencies [24,25], optimizing frequency allocation [23–25,32], and decreasing qubit connectivity [24,33], as shown, for example, in Fig. 1. Basically, as the quantum crosstalk comes from the always-ON interqubit coupling, lowering the strength can suppress it. However, this will lead to slow two-qubit gates, increasing gate errors from qubit decoherence. Thus, it is highly desirable to find a better solution to address this crosstalk issue without sacrificing gate speeds and fidelities.

Going beyond the CR architecture with fixed-frequency transmons and fixed couplings, several architectures have been proposed for addressing this issue, such as coupling qubits with opposite-sign anharmonicity [34–36] or introducing frequency-tunable elements [37,38]. However, generally, these approaches will introduce new decoherence channels and increase the control complexity. Within the present CR transmon architecture, several alternative approaches have also been developed, such as using optimized pulses [13,39], the ac-Stark shift [36,40,41], and the multipath coupler [42,43], yet it is still an outstanding challenge for suppressing quantum crosstalk while maintaining fast, high-fidelity gates in a robust and scalable manner.

In this work, we introduce a CR architecture based on fixed-frequency transmons and fixed couplings, which can passively mitigate both quantum crosstalk and frequency-collision issues. In such architecture, transmon qubits are coupled by a bus resonator, as shown in Fig. 1(c). In particular, unlike the setting in other existing literature [14,18,21,44], here the qubit-resonator detuning is comparable to the qubit anharmonicity α_q and the qubit-resonator coupling g_{rq} is more than about an order of magnitude smaller than the anharmonicity, i.e., $|\alpha_q/g_{rq}| \gtrsim 10$, retaining the dispersive condition. For the typical transmon anharmonicity of -330 MHz, here, the qubit-resonator coupling is below 30 MHz. It is, in this sense, that we nickname it the “lightweight” resonator coupler.

Within the architecture, the lightweight coupler allows one to address two main challenges in scaling up qubits, i.e., the speed-fidelity trade-off imposed by ZZ crosstalk and frequency collisions due to fabrication uncertainty. For the former, as the coupler-mediated XY and ZZ couplings are mainly enabled by virtual transitions in subspaces with different excitations, i.e., one-excitation and two-excitation subspaces, respectively, this enables one to engineer quantum interference to mitigate ZZ coupling while retaining XY coupling to support fast CR gates [42–47]. For the latter, to ensure fast CR gates, the other existing literature often favors the operating regime with positive control-target detunings [29,48–50]. By contrast, here, even under conditions of negative control-target detunings, high-fidelity CR gates can still be achieved with gate speeds

comparable to those with positive detunings. As a result, besides the positive detuning regions, the proposed architectures allow one to go beyond the existing literature by operating the qubit system in negative detuning regions, thereby mitigating the frequency-collision issue further, as illustrated, for example, in Figs. 1(d) and 1(e).

In addition, to assess the practicality, we systematically analyze the performance of the direct CX (CNOT) gate [13,51] on multiqubit lattices and study the effect of the qubit frequency uncertainty on the gates, assuming state-of-the-art precision in setting frequencies [24]. We find that, while ZZ crosstalk and frequency collisions for neighboring qubits can be largely mitigated, frequency collisions beyond nearest-neighbor qubits can exist due to the presence of submegahertz couplings, and can degrade gate performance. In particular, the frequency collisions could be classified into two major types: type 1 is the *static* frequency collision, such as on-resonance couplings of next-neighboring qubits, which can lead to strong state hybridization, degrading individual qubit addressability; and type 2 is the *dynamic* frequency collision, e.g., CR drive-induced multiphoton transitions. To address such collisions, we provide an intuitive model mainly based on the dressed state picture for identifying the primary error source. Then, we show that, by optimizing system parameters or adding weak off-resonant drives to selectively shift the qubits [40,41,52–56], the leading frequency collisions can be avoided.

The rest of the paper is organized as follows. In Sec. II A, we first provide a brief overview of CR-gate-based transmon architectures and then discuss ZZ crosstalk and frequency collisions. In Sec. II B, we give detailed descriptions of the introduced architecture, mainly focusing on ZZ suppression and revisiting the negative control-target detuning regime, which is previously identified as a slow gate regime. Within the architecture and assuming typical parameters, in Sec. III, we numerically analyze the performance of CX gates, including both isolated and

simultaneous gates, on multiqubit lattices. Moreover, we also examine the impact of frequency uncertainty on gates. In Sec. IV, we provide discussions of frequency collisions and the resulting challenges to be faced when scaling up the architecture. Finally, in Sec. V, we provide a summary of our work.

II. CR ARCHITECTURE WITH “LIGHTWEIGHT” RESONATOR COUPLER

In this section, for easy reference and to set the notation, we first briefly review the basic principle of CR gates and discuss the issues of ZZ crosstalk and the frequency collision in CR-gate-based transmon architectures. Then, we give a detailed description of the introduced architecture and show how it can address the two issues.

A. Overview of the CR-gate-based transmon architecture

1. Fixed-coupled transmons and effective Hamiltonians

The CR gate is an all-microwave-activated two-qubit gate for fixed-coupled qubits, and, within the CR architecture based on fixed-frequency transmons, qubits can be fixedly coupled via a coupling capacitor or a bus resonator, as depicted in Figs. 1(b) and 1(c). Note here that, for real qubit devices with capacitive coupling, besides the desired couplings, stray couplings, due to stray capacitances or effective capacitances mediated by coupling circuits [34, 57–59], can exist and have non-negligible contributions to interqubit couplings.

By considering this, Table I lists four main types of architectures for coupling transmons, which can be described by the static Hamiltonian (hereinafter, $\hbar = 1$)

$$H = H_0 + H_{\text{int}}, \quad (1)$$

$$H_0 = \sum_{q=1,2} \left(\omega_q a_q^\dagger a_q + \frac{\alpha_q}{2} a_q^\dagger a_q^\dagger a_q a_q \right) + \omega_r a_r^\dagger a_r. \quad (2)$$

TABLE I. Typical qubit parameters and approximations used in analyzing CR-gate-based transmon architectures. Here, the qubit parameters are similar to those extracted from experimental works and the coupling strength is given with the reference frequency of 5 GHz. In column (a), qubits are coupled directly via a capacitor [20]. In column (b), qubits are coupled via a resonator [18]. Here, to account for results in Ref. [18], direct coupling due to an effective capacitance is also taken into consideration [34,57]. In column (c), qubits are coupled via a multipath coupler [42,43,58]. In column (d), qubits are coupled by the lightweight resonator coupler introduced in the present work. Additionally, to reduce computation costs while maintaining sufficient accuracy, especially for analyzing multiqubit systems, the rotating-wave approximation is employed for columns (b) and (d).

Layout	Coupler			
	(a) Capacitor	(b) Resonator	(c) Multipath	(d) Lightweight resonator
Qubit-resonator coupling, $g_{rq}/2\pi$ (MHz)	0	78	78	25
Qubit-resonator detuning, $\Delta_q/2\pi$ (GHz)	...	1.0	1.0	0.25
Qubit-qubit coupling, $g_{12}/2\pi$ (MHz)	~ 2	$2g_{r1}g_{r2}/\omega_r$	6	0
Qubit anharmonicity, $\alpha_q/2\pi$ (MHz)	-330	-330	-330	-330
Rotating-wave approximation	with	without	without	with

Here ω_q and α_q are the frequency and the anharmonicity of transmon Q_q with the annihilation (creation) operator a_q (a_q^\dagger), and ω_r is the frequency of the resonator with the annihilation (creation) operator a_r (a_r^\dagger). The interaction Hamiltonian is

$$H_{\text{int}} = \sum_{\substack{q,p=1,2,r \\ q \neq p}} g_{qp} (a_q + a_q^\dagger)(a_p + a_p^\dagger), \quad (3)$$

where g_{r1} (g_{r2}) denotes the strength of the coupling between the resonator (R) and qubit Q_1 (Q_2), while g_{12} is the direct qubit-qubit coupling strength.

Truncated to the computational subspace, the static system Hamiltonian can be approximated by an effective Hamiltonian based on the two-level qubit model and is given as [43,50]

$$\tilde{H} = \tilde{\omega}_1 \frac{ZI}{2} + \tilde{\omega}_2 \frac{IZ}{2} + J_{xy} \frac{XX + YY}{2} + \zeta_{zz} \frac{ZZ}{4}, \quad (4)$$

where (X, Y, Z, I) denote the Pauli operators and $\tilde{\omega}_q$ is the dressed qubit frequency. Here, the third term describes the XY coupling resulting from the direct qubit-qubit coupling and the resonator-mediated indirect coupling, and, accordingly, the net coupling strength can be approximated by [58]

$$\begin{aligned} J_{xy} &= J_{\text{direct}} + J_{\text{indirect}}, \\ J_{\text{direct}} &= g_{12}, \\ J_{\text{indirect}} &= \frac{g_{r1}g_{r2}}{2} \left(\frac{1}{\Delta_1} + \frac{1}{\Delta_2} \right), \end{aligned} \quad (5)$$

where $\Delta_q = \omega_q - \omega_r$ denotes the qubit-resonator detuning. The last term is ZZ coupling, which results mainly from the interactions among two-excitation subspaces spanned by $\{|101\rangle, |200\rangle, |020\rangle, |002\rangle\}$ (hereafter, the two-qubit system state is denoted by the notation $|Q_0, R, Q_1\rangle$) and is defined as [26,57]

$$\zeta_{zz} = (E_{101} - E_{100}) - (E_{001} - E_{000}), \quad (6)$$

where E_{mnl} denotes the eigenenergy of the static Hamiltonian of Eq. (1) with eigenstate $|mnl\rangle$ and $m, n, l = \{0, 1\}$. Note that qubit operations, such as gate operations and measurements, are commonly performed in terms of the eigenbasis of static (idle) Hamiltonians (see, e.g., Ref. [57]); hereinafter, our analysis thus takes this into consideration implicitly.

As the direct qubit-qubit coupling in general is far smaller than the qubit-resonator coupling, the ZZ coupling

strength can be approximated as [43,45]

$$\begin{aligned} \zeta_{zz} &\simeq \zeta_{200} + \zeta_{002} + \zeta_{020}, \\ \zeta_{200} &= \frac{-J_{002}^2}{\Delta + \alpha_1} \quad \text{with } J_{002} \simeq \sqrt{2}J_{xy}, \\ \zeta_{020} &= \frac{J_{200}^2}{\Delta - \alpha_2} \quad \text{with } J_{200} \simeq \sqrt{2}J_{xy}, \\ \zeta_{002} &= \frac{J_{020}^2}{\Delta_1 + \Delta_2} \quad \text{with } J_{020} \simeq \sqrt{2}J_{\text{indirect}}, \end{aligned} \quad (7)$$

where $\Delta = \omega_1 - \omega_2$ is the qubit detuning and each term comes from the interaction between the qubit state $|101\rangle$ and the high-energy states $\{|200\rangle, |020\rangle, |002\rangle\}$ with the corresponding coupling strengths $\{J_{200}, J_{020}, J_{002}\}$.

2. CR gate speed and ZZ crosstalk

Here we now turn to briefly review the CR gate scheme for the coupled transmons discussed above (for more details, we refer the reader to Refs. [29,48,50]). The CR gate is implemented by applying a microwave drive, i.e., CR drive, to the control qubit at the target qubit frequency. For the two-qubit system described by the Hamiltonian in Eq. (1), we consider that Q_1 is the control qubit while Q_2 is the target, thus giving the following drive Hamiltonian:

$$H_d = \Omega_d(t) \cos(\omega_d t + \phi_0)(a_1 + a_1^\dagger), \quad (8)$$

where ω_d is the drive frequency, and $\Omega_d(t)$ and ϕ_0 are the drive amplitude and initial phase, respectively. For simplicity, hereafter, we have $\phi_0 = 0$.

Before going into details of CR gates based on Eq. (8), we consider a more simple drive model based on the effective two-qubit system described by Eq. (4), giving

$$\tilde{H}_d = \Omega_d(t) \cos(\omega_d t) XI. \quad (9)$$

As we will show, this model allows for a concise picture of the relation between CR gate speeds and ZZ crosstalk, and, by combining with the following analysis based on Eqs. (1) and (8), this model will provide a direct insight into the effect of the qubit high-energy levels on CR gates.

By diagonalizing the effective Hamiltonian in Eq. (4) and then rewriting the drive Hamiltonian of Eq. (9) in the eigenstates, the full system Hamiltonian can be approximated by [8]

$$\begin{aligned} \bar{H}_{\text{full}} &= \bar{\omega}_1 \frac{ZI}{2} + \bar{\omega}_2 \frac{IZ}{2} + \zeta_{zz} \frac{ZZ}{4} + \bar{H}_d, \\ \bar{H}_d &= \Omega_d(t) \cos(\omega_d t) \left[XI + \frac{J_{xy}}{\Delta} ZX \right], \end{aligned} \quad (10)$$

where $\tilde{\Delta} = \tilde{\omega}_1 - \tilde{\omega}_2$ is the dressed detuning. Here, the XI term denotes the off-resonance drive on the control qubit,

mainly shifting the qubit frequency and thus finally contributing to a ZI term, while the ZX term is the core of the gate scheme, enabling CR (ZX) gates with gate speeds determined by the prefactor $\Omega_d J_{xy}/\Delta$. Note that, to mitigate the off-resonance error on the control qubit [51], the drive amplitude is generally smaller than the qubit detuning; thus the gate speed can be limited by the interqubit coupling J_{xy} .

In Eq. (10), as the ZZ term does not commute with the ZX term, it can degrade CR gates. To be more specific, for the typical CR architecture with capacitor or resonator couplers (see Table I), Eqs. (5) and (7) suggest that the ZZ coupling strength is typically an order smaller than the XY coupling strength. And to mitigate the error induced by the XI term in Eq. (10), the gate speed should be below J_{xy} . Considering these findings, typically, an XY coupling of 1.25 MHz can allow for a 200-ns CX gate and meanwhile leads to a residual ZZ coupling of ~ 125 kHz, which contributes a gate error of ~ 0.004 (note that this is only a rough estimation without considering the effect of high-energy levels on gate speeds) [42]. Moreover, the ZZ term can also cause idle errors and degrade individual qubit addressability [27,28]. In this sense, the ZZ coupling acts as quantum crosstalk, degrading the operational fidelity in CR architectures. Indeed, according to Eq. (7), while the crosstalk can be suppressed by decreasing the interqubit coupling, this, in turn, slows down the CR gate speed. In essence, this means that there exists a speed-fidelity trade-off imposed by the ZZ crosstalk.

In the above discussion, while the effect of the high-energy levels has been taken into account in analyzing ZZ crosstalk, their effect on the CR gate speed has not been explored. Here, based on the drive Hamiltonian, Eq. (8), we summarize the main results on this subject. To simplify the analysis, we consider that two transmons are coupled directly via a capacitor coupler, as indicated in Table I, and the static system Hamiltonian is given by Eq. (1) with $g_{rq} = 0$. Again, by rewriting the drive Hamiltonian in the eigenstates of the static Hamiltonian and then truncating to the qubit subspace, the drive Hamiltonian has the approximate form

$$\bar{H}_d = \Omega_d(t) \cos(\omega_d t) [XI + \mu_{ix}IX + \mu_{zx}ZX], \quad (11)$$

where the prefactors of the IX and ZX terms are

$$\begin{aligned} \mu_{ix} &= \langle \overline{101} | (a_1 + a_1^\dagger) | \overline{100} \rangle + \langle \overline{001} | (a_1 + a_1^\dagger) | \overline{000} \rangle, \\ \mu_{zx} &= \langle \overline{101} | (a_1 + a_1^\dagger) | \overline{100} \rangle - \langle \overline{001} | (a_1 + a_1^\dagger) | \overline{000} \rangle. \end{aligned} \quad (12)$$

By expanding to the first order in J_{xy}/Δ , the above expressions can be approximated by [29,48,50]

$$\mu_{ix} = \frac{-J_{xy}\Delta}{\Delta(\alpha_1 + \Delta)} \quad \text{and} \quad \mu_{zx} = \frac{J_{xy}\alpha_1}{\Delta(\alpha_1 + \Delta)}. \quad (13)$$

From Eqs. (10)–(13), different from the result based on the two-level qubit model, there exists an additional term IX , which commutes with the ZX term and thus does not degrade the CR gate and its speed. Importantly, assuming fixed J_{xy} , for positive control-target detunings, μ_{zx} , can have a larger magnitude than that with negative detunings, due to the negative transmon anharmonicity. As a result, to ensure fast gates, the positive detuning is favored while the negative detuning is identified as the slow gate condition [23,24]. Besides, from Eq. (13), μ_{zx} can be suppressed with large detunings. Thus, the straddling regime, i.e., $0 < \Delta < -\alpha_1$ [9], is often preferred for fast CR gates. Note that assuming an infinite anharmonicity $\alpha_1 \rightarrow \infty$, the above expression reduces to Eq. (10), confirming that the main difference between the result based on the two-level qubit model in Eq. (4) and the result shown here comes from the qubit high-energy levels.

3. Frequency collisions and frequency allocation

The above discussions mainly focus on the most basic unit, which comprises two fixed-frequency transmons with fixed coupling, of CR-gate-based transmon architectures. Here, we briefly discuss one of the most fundamental challenges in scaling up this architecture, i.e., frequency collisions. To start, we consider a fixed-coupled system of three transmons, labeled by Q_i , Q_j , and Q_k , as shown in Fig. 1(a), where Q_j is the control and Q_i and Q_k are targets. We further assume that the typical interqubit coupling and the detuning for control-target qubit pairs are J and Δ , respectively, and the typical CR drive magnitude is Ω . As mentioned above, to ensure fast gates, the qubit system is operated with positive control-target detunings ($\omega_j > \omega_{i(k)}$) in the straddling regime.

Generally, frequency collisions can be classified into two major types: *static frequency collision* due to always-ON couplings and *dynamic frequency collision* related to CR drive-induced transitions. As in the existing literature [23,24], here we list six main types of frequency collisions (S1, S2, D1–D4), which are caused by qubit-qubit couplings with strengths of $\sim J$ and by transitions with rates of $\sim J\Omega/\Delta$ or $\sim \Omega^2/\Delta$ (to achieve high-fidelity gates, these couplings and transitions give larger collision bounds than that arising from even higher-order couplings and transitions with strengths of, e.g., J^2/Δ and $J^2\Omega^2/\Delta^3$, which will be discussed in Sec. III):

(1) *Static frequency collision*. Because of the always-ON couplings: (i) for the static systems, any degeneracy in qubit state transitions, such as $|0\rangle \leftrightarrow |1\rangle$, can lead to a strong state hybridization between qubits, degrading individual qubit addressability; and (ii) for systems under CR drives, off-resonance drive can shift qubit frequencies and can cause qubits on-resonance with others, resulting in population swaps between qubits. For neighboring qubits

with coupling strengths of $\sim J$, there exist two most likely cases: (S1) $\omega_j = \omega_{i(k)}$, and (S2) $\omega_j = \omega_{i(k)} + \alpha_{i(k)}$.

(2) *Dynamic frequency collision*. This arises from unwanted transitions activated by CR drives and thus both the transition rates and the collision conditions (i.e., considering that the drive itself can Stark-shift system energy levels) depend on the drive. For a CR gate applied to Q_j and Q_i , a drive at the frequency of Q_i should be applied to Q_j . For Q_j itself, when the drive is on-resonance with its transitions, this will lead to three collisions, and two of the three also cause the static collisions, i.e., (S1) and (S2) (note that, depending on the specific (static or dynamic) situation, there should be different bounds on Δ in achieving high-fidelity gates). The newly added one is: (D1) the two-photon transition $|0\rangle \leftrightarrow |2\rangle$ with the condition of $\omega_{i(k)} = \omega_j + \alpha_j/2$. Besides, similar to Q_i , the drive can also be felt by the neighboring spectator Q_k , due to the always-ON coupling between Q_j and Q_k . Thus, when the frequency of Q_i , i.e., the CR drive frequency, is on-resonance with any transitions of Q_k , this can cause unwanted transitions of Q_k . This leads to two collision cases: (D2) the transition $|0\rangle \leftrightarrow |1\rangle$ with $\omega_i = \omega_k$, and (D3) the transition $|1\rangle \leftrightarrow |2\rangle$ with $\omega_i = \omega_k + \alpha_k$ ($\omega_k = \omega_i + \alpha_i$). Finally, there exists another condition: (D4) $2\omega_j + \alpha_j = \omega_i + \omega_k$, which corresponds to the drive-assisted transition $|100\rangle(|001\rangle) \leftrightarrow |020\rangle$.

From the above discussion, one can find that, similar to the ZZ crosstalk, these frequency-collision issues mainly arise from the always-ON interqubit couplings and the weak anharmonicity of transmons. More importantly, most of them can act as quantum crosstalk, limiting gate performance and imposing speed-fidelity trade-offs. Thus, to ensure fast, high-fidelity operations for multiqubit lattices, these frequency-collision conditions should be avoided, further reducing the usable frequency range determined by the weak transmon anharmonicity. For example, assuming a typical 250 ns CR gate, the qubit-qubit couplings and the rates of the drive-induced transitions are generally of the order of 1 MHz; thus, to ensure gate error of ~ 0.01 (0.001), the qubit system should be operated outside of the bound of about ± 10 MHz (± 30 MHz) around each frequency collision.

To this end, scaling up the CR-gate-based transmon architectures requires a minimum of five distinct frequencies, i.e., $\omega_5 > \omega_4 > \omega_3 > \omega_2 > \omega_1$, for square qubit lattices [23,24,33], while for heavy-hexagonal qubit lattices, as shown in Fig. 1(a), a minimum number of three, i.e., $\omega_3 > \omega_2 > \omega_1$, is required [24,33]. However, considering fabrication uncertainty, whether such frequency allocation can successfully mitigate frequency collisions depends on how precise the setting of qubit frequencies is, as shown, for example, in Fig. 1(d). Recent studies show that, for a heavy-hexagonal qubit lattice, the state-of-the-art precision in setting frequencies allows the CR architecture to scale up to the 100-qubit size while roughly a factor

of 2 further improvement is needed for 1000-qubit size [24]. Overall, these findings suggest that frequency collision is still the major challenge for scaling up the CR-based transmon architecture.

B. CR architecture with passive mitigation of ZZ crosstalk and frequency collisions

As discussed above, in the context of CR-gate-based transmon architecture, quantum crosstalk and frequency collisions are two major challenges to be faced when scaling up this architecture. In the following discussion, we will show how to passively mitigate both issues by introducing a promising CR architecture based on lightweight resonator couplers. Additionally, note that, as mentioned before, the straddling regime is preferred to ensure fast CR gates. Thus, hereafter, unless otherwise specified, we always consider this implicitly.

1. System Hamiltonian and ZZ suppression

As mentioned in Sec. I, in our proposed CR architecture, the fixed-frequency transmon qubits are coupled via a lightweight resonator, and the typical coupling parameters are tabulated in column (d) of Table I. For two transmons coupled via such a coupler, the static system Hamiltonian can be described by Eq. (1) with $g_{12} = 0$. After applying the rotating-wave approximation (RWA), the Hamiltonian is given by

$$H_{\text{static}} = \sum_{q=1,2} \left(\omega_q a_q^\dagger a_q + \frac{\alpha_q}{2} a_q^\dagger a_q^\dagger a_q a_q \right) + \omega_r a_r^\dagger a_r + \sum_q g_{rq} (a_r a_q^\dagger + a_r^\dagger a_q). \quad (14)$$

As in Sec. II A, truncated to the qubit subspace, the above Hamiltonian can be approximated by Eq. (4) with the XY and the ZZ coupling strengths given as [26]

$$J_{xy} = J_{\text{indirect}} = \frac{g_r g_{r2}}{2} \left(\frac{1}{\Delta_1} + \frac{1}{\Delta_2} \right), \quad (15)$$

$$\zeta_{zz} = 2J_{xy}^2 \left[\frac{1}{\Delta - \alpha_2} - \frac{1}{\Delta + \alpha_1} + \frac{1}{\Delta_1 + \Delta_2} \right].$$

Note that, as already mentioned in Sec. II A, stray couplings between qubits are ubiquitous in real devices. In Appendix A, we provide specific cases for illustrating their effects in the currently studied architecture and show that their presence does not change the main results based on Eq. (14). Accordingly, in the following discussion, to avoid repetition, we will focus only on the qubit architecture described by Eq. (14), in which the direct qubit-qubit coupling is not included.

From Eq. (15), there are two essential features in the current architecture: (1) a ZZ-free point can exist due to

the destructive interference of ZZ coupling contributing from interactions between computational state $|101\rangle$ and high-energy states $\{|200\rangle, |002\rangle, |020\rangle\}$ [45,46,60]; and (2) its existence does not depend on the XY coupling strength J_{xy} . The two features allow us to suppress ZZ coupling while retaining XY coupling. For instance, considering that when the qubit detuning is far smaller than the qubit anharmonicity (i.e., $|\Delta| \ll |\alpha_q|$), according to Eq. (15), the ZZ-free point exists when the qubit-resonator detuning is comparable to the qubit anharmonicity, i.e., $\Delta_q \simeq \alpha_q$. Accordingly, the strength of the maintained XY coupling is about $g_{r1}g_{r2}/\alpha_q$. For the typical transmon anharmonicity of -330 MHz and within the dispersive regime, i.e., $|\Delta_q/g_{rq}| \gtrsim 10$, XY couplings with the strengths of 1–3 MHz can be obtained, potentially allowing fast CR gates.

By contrast, according to Eqs. (7) and (15), the ZZ expression for direct-coupled qubits is then expressed as [61]

$$\zeta_{zz} = 2J_{xy}^2 \left[\frac{1}{\Delta - \alpha_2} - \frac{1}{\Delta + \alpha_1} \right] \quad \text{with } J_{xy} = g_{01}, \quad (16)$$

which illustrates that no ZZ-free point exists in the direct-coupled architectures. Meanwhile, for the architecture with resonator couplers shown in Table I, when one allows this architecture to be operated outside of the dispersive regime, i.e., quasi-dispersive regime, $|\Delta_q/g_{rq}| < 10$, the ZZ coupling can also be suppressed while maintaining even larger XY couplings [44,46]. However, in this situation, besides the fact that ZZ suppression depends strongly on system parameters (e.g., is very sensitive to small drifts in qubit and resonator frequencies), the strong state hybridization between qubits and the resonator will

degrade individual qubit addressability and aggravate the frequency-collision issues.

We now turn to give a more quantitative analysis of the introduced architecture. Moreover, for ease of comparison, we also show the results for the existing architectures tabulated in Table I. Within the CR architecture, Fig. 2 shows contour plots of the ZZ (filled contours) and XY (dashed contours) coupling strengths as functions of system parameters, with the control qubit frequency of 5.15 GHz and the other qubit parameters listed in Table I. Here, according to Eq. (6), ZZ coupling strengths are extracted by numerical diagonalization of the static system Hamiltonian, while, similar to Eqs. (12) and (13), XY coupling strengths are inferred from the following approximation [48]:

$$-\frac{J_{xy}}{\Delta} \simeq \langle 001 | (a_1 + a_1^\dagger) | 000 \rangle. \quad (17)$$

To verify this, Fig. 2(a) shows both the inferred J_{xy} values and the setting values, $J_{xy} = g_{12}$. One can note that the inferred values mostly agree well with the setting values. This justifies the estimation of J_{xy} based on Eq. (17).

From the results shown in Figs. 2(a) and 2(b), as expected, in architectures with capacitor or resonator couplers, no ZZ-free points exist and the ZZ coupling strength is typically 10-fold smaller than that of the XY coupling, giving rise to $|J_{xy}/\zeta_{zz}| \sim 10$. However, as shown in Fig. 2(d), for the lightweight resonator coupler, ZZ-free points exist and the ZZ coupling can be heavily suppressed in a wide frequency range while the maintained XY coupling strength typically ranges from 1 to 3 MHz. Remarkably, compared to the capacitor and resonator couplers, this gives rise to $|J_{xy}/\zeta_{zz}| > 10^2$, providing at least one order-of-magnitude improvement in ZZ suppression.

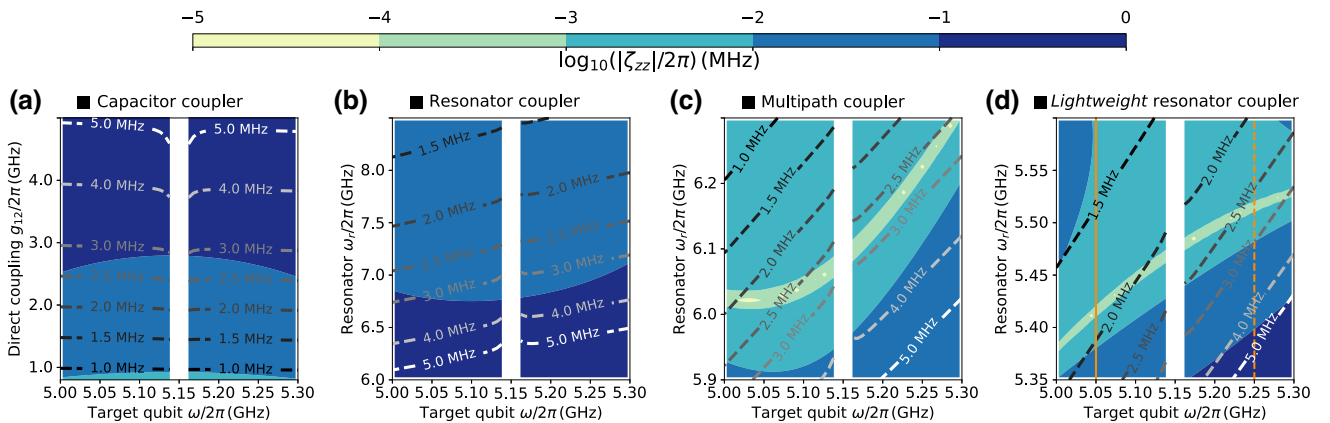


FIG. 2. Landscapes of ZZ coupling ζ_{zz} (filled contours) and XY coupling J_{xy} (dashed contours). Here, the control qubit frequency is $\omega_1/2\pi = 5.15$ GHz, and the coupling parameters and the qubit anharmonicity are listed in Table I. (a) For qubits coupled via capacitor couplers, the contours show the ZZ and XY coupling strengths as functions of the target qubit frequency and the direct coupling strength. (b)–(d) The ZZ and XY coupling strengths as functions of the target qubit frequency and the resonator frequency, for qubits coupled via (b) resonator couplers, (c) multipath couplers, and (d) the introduced lightweight resonator couplers, respectively. Vertical cuts, indicated by the solid and dashed orange lines, denote the result plotted in Figs. 3(a) and 3(b), respectively.

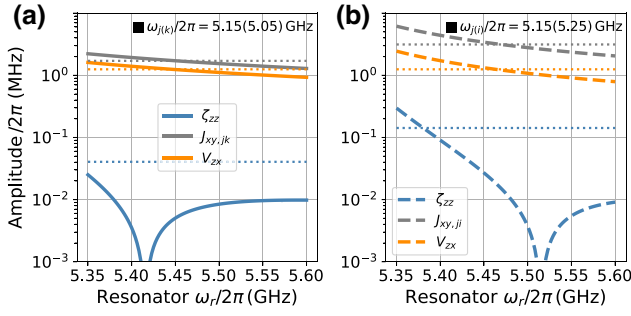


FIG. 3. The magnitudes of the ZZ coupling strength ζ_{zz} , the XY coupling strength J_{xy} , and the ZX rate V_{zx} (inferred by assuming a CR drive magnitude of 50 MHz) as functions of the resonator frequency in the proposed architecture. Here, plots of ζ_{zz} and J_{xy} denote two one-dimensional vertical cuts through Fig. 2(d) (indicated by the solid and dashed orange lines) at the target qubit frequencies of (a) $\omega_k/2\pi = 5.05$ GHz and (b) $\omega_i/2\pi = 5.25$ GHz, respectively, and at the control qubit frequency of $\omega_j/2\pi = 5.15$ GHz. The dotted lines represent the results for direct-coupled qubits with the target ZX rate of 1.25 MHz, allowing 200-ns CX gates without rise-fall times.

More specifically, vertical cuts through Fig. 2(d) at the target qubit frequencies of 5.05 and 5.25 GHz are shown in Fig. 3, where dotted lines denote the results for direct-coupled qubits with the target of ensuring 200-ns CX gates (assuming the CR drive amplitude of 50 MHz and ignoring rise-fall times). In contrast to the direct-coupled case, where the residual ZZ coupling strength is typically in the range of 50–100 kHz, the lightweight resonator coupler can allow the ZZ suppression to below 10 kHz, in both the positive [see Fig. 3(a)] and negative [see Fig. 3(b)] control-target detuning regions.

As shown in Fig. 2(c), and demonstrated in the previous works [42,43], similar improvements can also be available for architectures with multipath couplers. In particular, as the design of multipath couplers generally increases the circuit complexity, so their success on ZZ suppression is potentially more prone to imperfections attributable to the design itself and fabrications. Meanwhile, the result shown in Fig. 2(d) demonstrates that, even with a simpler coupling circuit, ZZ suppression could still be achieved while maintaining large XY couplings. However, note that the lightweight resonator coupler also has its own drawbacks as well, which will be discussed in Sec. IV.

2. Revisiting the slow gate region

The above discussions have illustrated that, with lightweight resonator couplers, ZZ crosstalk can be mitigated while maintaining large XY couplings. More importantly, in contrast to the cases with capacitor or resonator couplers [see Figs. 2(a) and 2(b)], here one can find a remarkably strong dependence of the XY coupling strength J_{xy} on the control-target detuning, as shown in Fig. 2(d).

This can be more specific, in that, as illustrated in Fig. 3, compared to that in positive detuning regions, a typical twofold increase in J_{xy} can be obtained without affecting the ZZ suppression within the negative detuning regions. As expected from Eq. (13), the increased XY coupling can compensate for the loss in gate speed due to the negative transmon anharmonicity. Therefore, fast CR gates could also be available within the negative detuning regions, which have previously been identified as forbidden zones with slower gate speeds [23,24].

The origin of the above appealing features can be rationalized by noting that from Eq. (15), when the qubit-resonator detuning is comparable to the qubit-qubit detuning (as in the currently studied architecture), i.e., $|\Delta_q| \sim |\Delta|$, then J_{xy} will depend strongly on the detuning sign. By assuming a fixed control qubit frequency, having negative control-target detunings means that the detuning between the resonator and the target qubit is smaller than that with positive detunings, enabling larger resonator-mediated XY couplings. By contrast, if $|\Delta_q| \gg |\Delta|$ (as in the architecture with resonator couplers), whether the detuning changes its sign, there is little effect on J_{xy} , as shown in Fig. 2(b). Therefore, in architectures with capacitor and resonator couplers, to increase XY coupling, one has to increase the direct coupling or the qubit-resonator coupling, and this will inevitably increase ZZ couplings. For example, under the conditions with negative detunings, to ensure gate speed comparable to that in the positive detuning regions, the direct coupling strength should be increased from 1.7 to 3.1 MHz and, accordingly, the ZZ coupling will increase from 41 to 142 kHz, as shown by the dotted lines in Fig. 3. This further explicitly explains why the negative detuning was previously identified as the slow gate condition [23,24]. On the contrary, here all the benefits from the increased XY coupling can be achieved without sacrificing ZZ suppression. Additionally, Fig. 2(c) also shows similar appealing behavior, suggesting that the multipath coupler can be an alternative for achieving fast gate speed in negative detuning regions.

In particular, Fig. 3 also shows the ZX rate V_{zx} as a function of the resonator frequency. Here, according to Eq. (12), V_{zx} is determined by

$$V_{zx} = \frac{1}{2}\Omega\mu_{zx}, \quad (18)$$

with the assumption of the CR drive magnitude $\Omega/2\pi = 50$ MHz. As expected, even under the condition of negative detunings, the resulting ZX rate is comparable to that within the positive detuning regions. While here the typical ZX rate is about 1 MHz, allowing 250-ns CX gates without rise-fall times, even higher ZX rates may be possible by increasing the qubit-resonator coupling g_{rq} . However, increasing g_{rq} generally will increase the residual ZZ couplings. For example, when increasing the qubit-resonator coupling from 25 to 30 MHz, the typical ZX rate becomes

1.5 MHz while the typical ZZ coupling has increased to 20 kHz (see Appendix B for details). Given that the state-of-the-art gate performance is still limited by qubit decoherence, presently unitizing larger qubit-resonator couplings could help increase the gate speed and reduce the incoherent error. This highlights the importance of balancing incoherent errors and coherence errors arising, for example, from ZZ crosstalk, to achieve high-fidelity gates.

Below, to provide a more direct verification, we turn to study the implementation of CX gates within the introduced architecture. In particular, we will focus on both the conditions of positive and negative control-target detunings. Here, based on the CR gate scheme, we consider the realization of direct CX gates [13,51]. Besides the CR drive on the control qubit, here, an additional cancelation drive is also applied to the target qubit at its frequency. This additional drive is introduced to ensure no operation on the target qubit when the control qubit is in state $|0\rangle$ [51]. Accordingly, within the RWA, the drive Hamiltonian can be expressed as

$$H_{\text{drive}} = \sum_{q=1,2} \frac{1}{2} \Omega_q(t) (a_1^\dagger e^{-i\omega_d t} + a_1 e^{i\omega_d t}), \quad (19)$$

where $\Omega_q(t)$ denotes the amplitude of the drive on Q_q . Hereafter, we consider using cosine-decorated square pulses with fixed ramp times of 20 ns, which are defined as

$$\Omega_d(t) \equiv \begin{cases} \frac{1}{2} \Omega \left[1 - \cos\left(\pi \frac{t}{t_r}\right) \right], & 0 < t < t_r, \\ \Omega, & t_r < t < t_g - t_r, \\ \frac{1}{2} \Omega \left[1 - \cos\left(\pi \frac{t_g - t}{t_r}\right) \right], & t_g - t_r < t < t_g, \end{cases} \quad (20)$$

where Ω denotes the peak drive amplitude, $t_r = 20$ ns is the ramp time, and t_g represents the gate length. A detailed procedure on the gate tune-up and the characterization for the CX gate can be found in Appendix C.

Figure 4 shows both the CX gate error (intrinsic error, i.e., excluding the gate error from qubit incoherence) [62] and the CR drive amplitude as functions of the gate length with varying resonator frequencies. As expected from the above analysis, under the conditions of negative detunings, high-fidelity CX gates can still be achieved with a gate speed comparable to that within the positive detuning regions. Moreover, the results shown in Fig. 4 also illustrate that, within the typical range of 20–70 MHz drive amplitude, CX gates with gate errors approaching 10^{-4} could be obtained with a gate length of 250–450 ns. In addition, as studied in previous works [51,63–65], by optimizing the drive parameters, the pulse ramp time can be shorter and the off-resonance error due to the CR drive

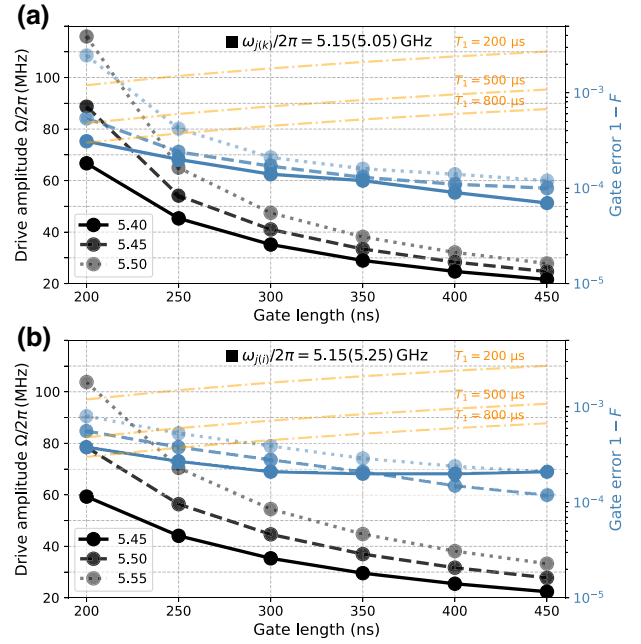


FIG. 4. CX gate errors (in the absence of decoherence) and peak drive amplitudes as functions of the gate length with varying resonator frequencies. Here, the control qubit frequency is $\omega_j/2\pi = 5.15$ GHz, and the coupling parameters and the qubit anharmonicity are listed in Table I. Orange dash-dotted lines denote the incoherence error ϵ_{incoh} versus the gate length (the coherence times are assumed to be the same for both the control and target qubits and $T_2 = T_1$, with different T_1). (a) The target qubit frequency is $\omega_k/2\pi = 5.05$ GHz, giving rise to the condition of positive control-target detunings. (b) The target qubit frequency is $\omega_k/2\pi = 5.25$ GHz, giving rise to the conditions of negative control-target detunings.

can be further suppressed. Moreover, as mentioned before, even higher ZX rates (e.g., 1.5 MHz, allowing for a 200-ns CX gate with a ramp time of 20 ns) can be obtained by increasing the qubit-resonator coupling. Meanwhile, the resulting ZZ coupling can be suppressed below 20 kHz, contributing to the gate error at the level of 10^{-4} [42]. Thus, CX gates with even faster gate speed and higher gate fidelity should be possible within the currently studied CR architecture.

Furthermore, in Fig. 4, we also show the incoherence error versus the gate length for the CX gate. Here, the coherence times are assumed to be the same for both the control and target qubits with $T_2 = T_1$ [12,51], and the incoherence error can be estimated by $\epsilon_{\text{incoh}} \approx \sum_{q=1,2} [\frac{1}{5}(t_g/T_1^{(q)}) + \frac{2}{5}(t_g/T_2^{(q)})]$ [51]. One can clearly see from Fig. 4 that there exists a trade-off between the intrinsic (control) gate error (mainly dominated by the control error from the off-resonance CR drive) and the incoherence error. Given the state-of-the-art coherent times of fixed-frequency qubits [15–17], the gate error should be limited

by the qubit incoherence in both the negative and positive detuning regimes.

As in various qubit architectures with superconducting qubits, gate speeds and operational performance generally hinge on the ability in setting qubit parameters. Specifically, in the currently studied CR architecture and for fixed resonator-qubit couplings (see Figs. 3 and 4), the gate speed is mainly determined by the qubit-resonator detuning. Accordingly, assuming the drive amplitude of 50 MHz, to ensure 300-ns CX gates (with a ramp time of 20 ns), the usable range of the qubit-resonator detuning is about 200 MHz for the positive detuning case, while it reduces to about 100 MHz for the negative detuning case, as shown in Figs. 3 and 4. In contrast to the architecture with resonator couplers, where the XY coupling (thus also the CR gate speed) shows less sensitivity to the variation in qubit-resonator detuning [see Fig. 2(b)], this generally introduces an additional constraint for achieving fast CR gates. However, as illustrated in Appendix B, increasing resonator-qubit couplings could help relieve this constraint. Moreover, since currently the reproducibility of the resonator frequency is much better than that of qubits (see, e.g., Ref. [66]), this constraint could be largely addressed by improving the accuracy in setting qubit frequencies (as for addressing the frequency-collision issue, but with less stringent requirements on accuracy).

Given the above illustration of fast CX gates in the negative detuning region, we now go back to the frequency-collision issue. As discussed in Sec. II A, the qubit frequency allocation should be optimized to balance gate errors due to frequency collisions and incoherence errors resulting from slow gate speeds. Since, currently, gate performance is most likely to be limited by qubit decoherence, the positive detuning region is preferred for ensuring fast gates. However, this in turn decreases the usable range of qubit detunings, making the frequency-collision issue more prominent. Thus, mitigating frequency collisions and improving the collision-free yield of large-size systems put stringent requirements on the accuracy in setting qubit frequencies [23,24,32]. Even with sparse connectivity, e.g., the heavy-hexagonal lattice topology shown in Fig. 1(a), the state-of-the-art accuracy is still not enough to support 1000-qubit systems [24]. Within the currently studied CR architecture, we show that fast gates are also available in the negative detuning regions, extending the usable detuning range. As a consequence, we expect that this could largely mitigate the frequency-collision issue and relax the stringent requirement on the accuracy for scaling up to large system sizes.

III. CROSSTALK MITIGATION IN MULTIQUBIT SYSTEMS

In this section, to examine the practicality of the architecture, we intend to investigate the CX gate performance

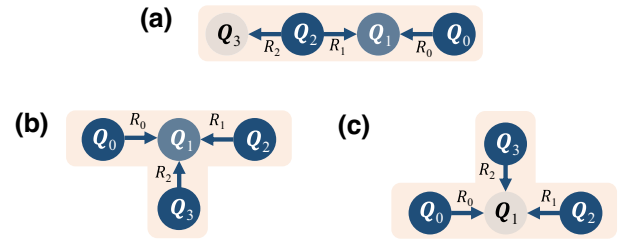


FIG. 5. Typical four-qubit units in the heavy-hexagonal qubit lattice with the three-frequency pattern shown in Fig. 1(a). The three four-qubit systems, i.e., (a) “-” shape, (b) “T” shape, and (c) “L” shape, are also shown in the pale shading in Fig. 1(a). Here, the arrows indicate the direction of the CR gates, i.e., from control to target.

and the impact of quantum crosstalk on it in the typical four-qubit units of the heavy-hexagonal qubit lattice, as shown in Fig. 5. Then, we turn to give schemes mitigating the crosstalk effect on gates. As shown in Fig. 1(e), unlike in other existing literature [see Fig. 1(d)], here the three-frequency pattern is given as $\omega_i > \omega_j > \omega_k$. Following the above discussion, here we consider that the desired control frequency is $\omega_j/2\pi = 5.15$ GHz while the target qubit frequency is $\omega_{i(k)}/2\pi = 5.25$ (5.05) GHz. This frequency allocation scheme is expected to mitigate the frequency-collision issue within the current architecture, as illustrated in Figs. 1(d) and 1(e).

In the following discussion, we first study the gate performance of isolated CX gates in the four-qubit systems and then turn to study the simultaneous gates. Moreover, we also provide a preliminary study to determine the effect of frequency variations on ZZ suppression and gate performance.

A. Error analysis with typical qubit parameters

1. Isolated CR gates

Given the system parameters listed in Table II, Fig. 6 shows both the isolated gate error $1 - F$ and leakage L_1 [67] as functions of the gate length for the three four-qubit systems shown in Fig. 5. Here, the ZZ coupling between near-neighbor qubits ranges from 1 to 13 kHz and is expected not to limit the following CX gate performance.

TABLE II. Typical qubit and resonator parameters used in studying the four-qubit units shown in Fig. 5. The other system parameters are listed in Table I and the resulting ZZ couplings range from 1 to 13 kHz for near-neighbor qubits. Here, the qubit and resonator frequencies are given in units of gigahertz.

Layout	Q_0	R_0	Q_1	R_1	Q_2	R_2	Q_3
“-” shape	5.15	5.40	5.05	5.41	5.14	5.47	5.25
“T” shape	5.15	5.40	5.05	5.41	5.14	5.39	5.16
“L” shape	5.14	5.47	5.25	5.48	5.15	5.49	5.16

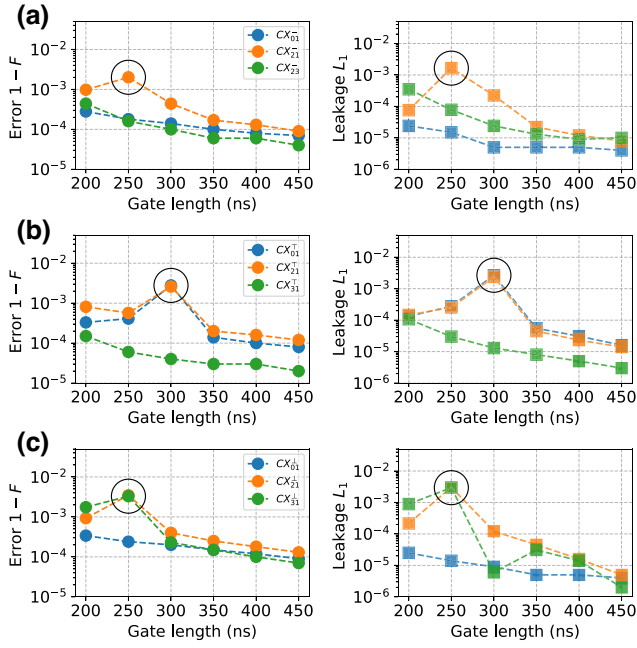


FIG. 6. The isolated gate error $1 - F$ (left panels) and leakage L_1 (right panels) as functions of the gate length. Panels (a), (b), and (c) correspond to the four-qubit systems shown in Figs. 5(a), 5(b), and 5(c), respectively. The used parameters are listed in Table II. Hereafter, for example, CX_{21}^- denotes the CX gate for the control qubit Q_2 and the target qubit Q_1 of the “-” shape four-qubit system shown in Fig. 5(a). The black circles highlight the spikes of gate errors and leakage.

Note that hereafter the isolated gates are characterized by assuming all the spectator qubits in their ground states [60]; see Appendix C for more details.

From the result shown in the left panels of Fig. 6, as expected, increasing the gate length can generally reduce gate errors (mainly due to the off-resonance CR drive [51,65]). However, unlike isolated two-qubit systems (see Fig. 4), the gate error can show spikes (highlighted by black circles) at specific gate lengths, which is coincident with the increase of leakage, as shown in the right panels of Fig. 6. For instance, in Fig. 6(a), the gate error of CX_{21}^- shows a spike at the gate length of 250 ns, coinciding with the peak of leakage. This suggests that the spikes of the gate error dominantly arise from leakage related to spectator qubits.

Inspired by the crosstalk analysis of baseband flux-based gate operations [60], here we use a similar approach based on the dressed states picture to identify the leading source of the isolated gate errors. Note that here we focus only on the driven system with a single drive frequency, while for driven systems with multiple distinct drive frequencies (i.e., related to simultaneous CR gates), the analysis given in Floquet theory could be devised for this purpose [31,68–70]. By moving into the rotating frame at the CR drive frequency and within the RWA, the full system

Hamiltonian, for example, describing the implementation of CX_{21}^- on the four-qubit system shown in Fig. 5(a), can be expressed by

$$H = \sum_q \left(\omega_q a_q^\dagger a_q + \frac{\alpha_q}{2} a_q^\dagger a_q^\dagger a_q a_q \right) + \sum_n (\omega_{r,n} a_{r,n}^\dagger a_{r,n}) + \sum_{q,n} [g_{r,nq} (a_{r,n} a_q^\dagger + a_{r,n}^\dagger a_q)] + \frac{\Omega}{2} (a_2^\dagger + a_2), \quad (21)$$

with the qubit and the resonator labeled by $q = \{0, 1, 2, 3\}$ and $n = \{0, 1, 2\}$, respectively. Here, to simplify the discussion, we neglect the cancelation drive term [see Eq. (19)].

By numerical diagonalization of the Hamiltonian in Eq. (21), Fig. 7(a) shows the dressed eigenenergies of the “-” shape four-qubit system under the drive on Q_2 as a function of the CR drive amplitude. One can find

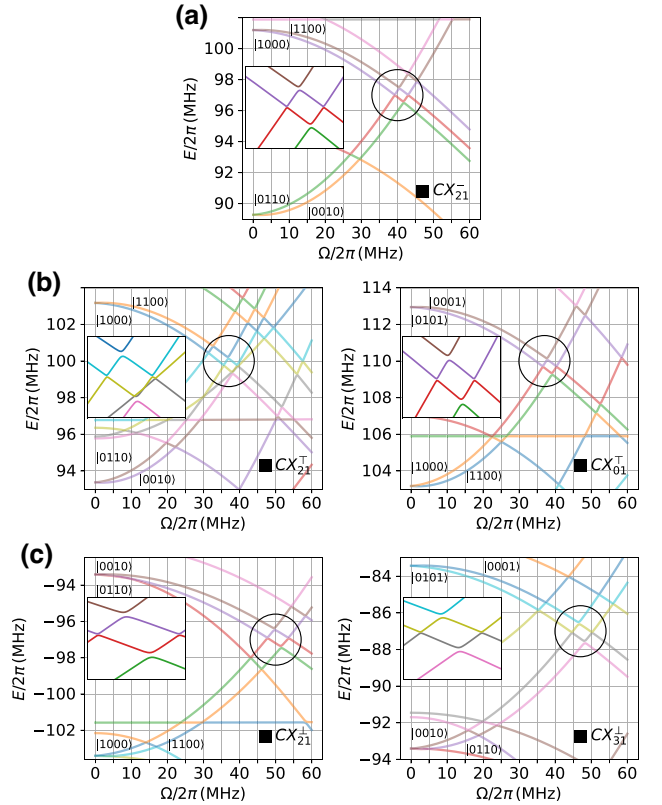


FIG. 7. Dressed spectrum of the four-qubit systems under the CR drive, showing the dressed eigenenergies of the driven system as a function of the CR drive amplitude. Here, the parameters used are the same as in Fig. 6. (a) For the “-” shape system with the drive applied to Q_2 . (b) The left and right panels denote the dressed spectrum for the “T” shape system with the drive applied to Q_2 and Q_0 , respectively. (c) The left and right panels denote the dressed spectrum for the “L” shape system with the drive applied to Q_2 and Q_3 , respectively. The insets enlarge the areas within the black circles and highlight the level anticrossings arising from next-nearest-neighbor interactions, which lead to the spikes of gate errors and leakage shown in Fig. 6.

that, near the drive amplitude of ~ 42 MHz, there exist level anticrossings arising from the resonance interaction between Q_2 and its next-nearest-neighbor Q_0 with the strength of ~ 55 kHz (in line with the strength of the next-nearest-neighbor interaction mediated by Q_1). Meanwhile, for CX_{21}^- with the gate length of 250 ns shown in Fig. 6(a), the peak drive amplitude is about 45 MHz [see also Fig. 4(a)]. These two observations indicate that, during the implementation of 250-ns CX_{21}^- , the qubit system is operated near the anticrossing, thus enabling the population swap between Q_2 and Q_0 and causing the increase in leakage and gate errors. By contrast, for shorter gates (e.g., 200 ns) or slower gates (e.g., 300 ns), the qubit system is operated far away from the anticrossing, allowing the suppression of the population swap. In this situation, the gate error and leakage will be restored to the level, which is limited mainly by the off-resonance error within the isolated two-qubit system itself, as illustrated in Fig. 6(a).

Similarly to CX_{21}^- , the spikes of gate error and leakage in the “T” shape and “L” shape four-qubit systems, as shown in Figs. 6(b) and 6(c), also arise due to the parasitic interactions between the control qubits and their next-nearest-neighbor qubits, highlighted in Figs. 7(b) and 7(c). Thus, in essence, the increased gate errors shown in Fig. 6 are caused by the static frequency collision resulting from the next-nearest-neighbor interaction, as discussed in Sec. II A.

2. Modeling the formation of frequency collisions

To get further insight into the underlying physics of the above collision processes, we consider a more intuitive model based on the dressed state picture. For a multilevel quantum system under an off-resonance drive, as shown in Fig. 8(a), moving into the rotating frame at the drive frequency gives a dressed multilevel system, whose spectrum as a function of the drive amplitude is sketched in Fig. 8(b). Through the ac-Stark effect, the off-resonance drive can shift the levels lower or higher in frequency, which is determined by whether or not the drive is blue-detuned or red-detuned from the transitions in the multilevel system. As a consequence, by increasing the drive amplitude, one shifted level can sweep through the other shifted one, as shown, for example, in Fig. 8(b). Furthermore, when the two levels are coupled together, there can exist a level anticrossing, whose size is determined by the coupling strength, at the resonance point, as shown in the inset of Fig. 8(c). Basically, these two factors together lead to the formation of frequency collisions. In this context, according to the primary mechanism underlying the coupling, the frequency collision can be classified into static or dynamic, as discussed in Sec. II A.

Similar to the above model, in the context of CR gate architecture, the off-resonance CR drive will shift the control qubit frequency, causing accidental frequency

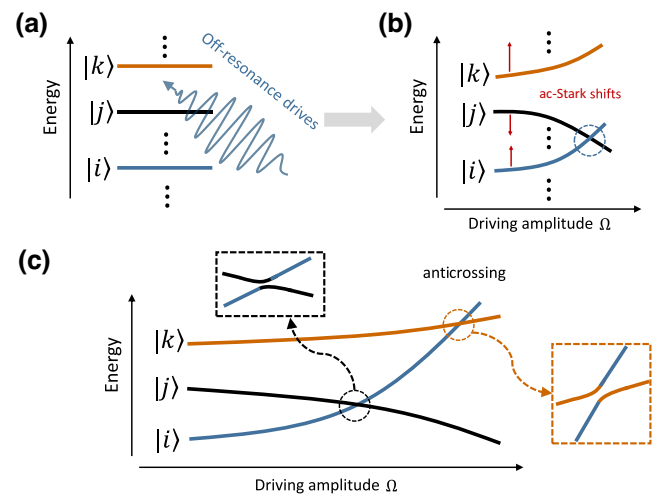


FIG. 8. Modeling the formation of frequency collisions based on the dressed state picture. (a) For a multilevel quantum system, wherein energy levels are labeled by $|i\rangle, |j\rangle, |k\rangle, \dots$, subjected to an off-resonance drive, moving into the rotating frame at the drive frequency can give a dressed system. (b) The typical dressed spectrum as a function of the drive amplitude, showing that, through the ac-Stark effect, the off-resonance drive can cause blue-shifted and red-shifted energy levels. When increasing the drive amplitude, the shifted levels, e.g., $|j\rangle$, can sweep through the others, e.g., $|i\rangle$. (c) Because of the interactions between levels, anticrossings (highlighted by insets) can exist at the resonance points.

collisions between the control qubit and its neighbors. Specifically, we consider the collision process underlying the results shown in Figs. 6 and 7. As listed in Table II, the typical magnitude of the control-target (i.e., near-neighboring qubit pairs) detuning is 100 MHz while the control qubit and its next-nearest neighbors (i.e., another control qubit) are only detuned by 10 MHz. Thus, given the typical drive amplitude of $\Omega/2\pi = 50$ MHz and the detuning magnitude of $\Delta/2\pi = 100$ MHz, the ac-Stark shift can be approximated by [71]

$$\delta_s \approx \frac{\alpha_q \Omega^2}{2\Delta(\Delta + \alpha_q)}, \quad (22)$$

giving rise to 16 MHz and -9 MHz for the positive and negative detuning conditions, respectively. Moreover, the control qubit and its next-nearest neighbors, e.g., Q_2 and Q_0 in Figs. 6(a) and 7(a), can be coupled via the mediator, e.g., Q_1 , with the typical strength of $\sim J^2/\Delta$ (see also Sec. II). Given these considerations, the static frequency collision due to the on-resonance coupling between neighboring control qubits can explicitly explain the presence of the spikes in gate errors and leakage at specific drive amplitudes shown in Fig. 6.

In essence, this frequency collision is caused by the always-ON qubit-qubit couplings (in this sense, we call it a static frequency collision). But the condition for the

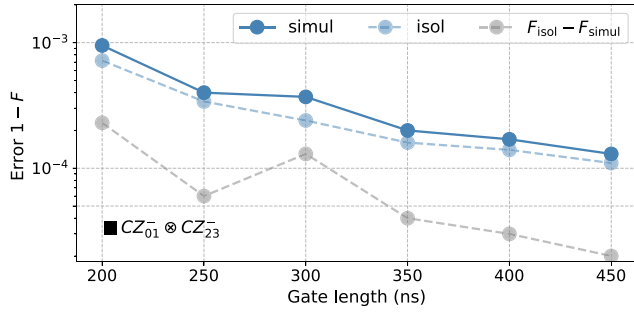


FIG. 9. Gate errors of the simultaneous CX gates ($CX_{01}^- \otimes CX_{23}^-$) in the “-” shape four-qubit system as a function of the gate length. Here, the parameters used are the same as in Fig. 6(a) and the isolated gate errors are obtained by adding the errors of the constituent isolated gates (i.e., CX_{01}^- and CX_{23}^-) shown in Fig. 6(a).

occurrence of such a collision depends on the CR drive amplitude (gate length). This in turn allows one to avoid such collision issues by optimizing drive amplitudes (gate lengths), as suggested in Fig. 6.

3. Simultaneous gate operations

To further examine whether there exists additional quantum crosstalk for implementing CX gates in parallel, here we provide an analysis of the fidelity of simultaneous CX gates [60]. With the typical parameters listed in Table II, Fig. 9 shows the performance of simultaneous gates ($CZ_{01}^- \otimes CZ_{23}^-$) in the “-” shape four-qubit system shown in Fig. 5(a). Here, by adding the errors of the constituent isolated gates CZ_{01}^- and CZ_{23}^- , we also show the isolated gate errors ($1 - F_{\text{isol}}$) and the added errors ($F_{\text{isol}} - F_{\text{simul}}$) when gates are implemented in parallel. Similar to isolated gates (see Fig. 6), increasing the gate length can reduce the simultaneous gate error. Moreover, the typical added error is below 10^{-4} , suggesting that there exists no additional quantum crosstalk that contributes significantly to gate errors. This shows that, within the currently studied CR architecture, high-fidelity simultaneous gates may be possible, but, as we will show, this is far from the whole story. We will go back to this subject in the following section.

B. Challenge from fluctuations in qubit parameters

Below, to study the effect of frequency uncertainty on the currently studied architecture, we consider that control and target qubit frequencies are randomly distributed around their designed values, i.e., the control frequency of $\omega_j/2\pi = 5.15$ GHz and the target frequency of $\omega_{i(k)}/2\pi = 5.25$ (5.05) GHz, with the standard deviation of $\sigma_f = 15$ MHz [24]. With 100 distinct repetitions, we provide analysis of both the ZZ suppression and the performance of CX gates (including both isolated gates

and simultaneous gates) for the four-qubit systems shown in Fig. 5. Accordingly, Figs. 10(a)–10(c) show the qubit frequencies of 100 repetitions for the four-qubit systems shown in Figs. 5(a)–5(c).

1. ZZ suppression

As shown in Fig. 3, for isolated two-qubit systems with the desired setting in qubit frequencies, the ZZ coupling can be suppressed below 10 kHz. However, as we will show, the deviation from the target setting in multiqubit systems will make the ZZ suppression more complicated.

Figures 10(d)–10(f) show the ZZ couplings of 100 repetitions; the maximum (median) values of the ZZ coupling are 26 (3), 38 (3), and 33 (7) kHz for the four-qubit systems shown in Figs. 5(a)–5(c), respectively. Moreover, it is also shown that the “exceptional” points with large ZZ couplings almost appear in pairs, as shown in Fig. 10(e). To check their dependence on the qubit frequencies, the insets

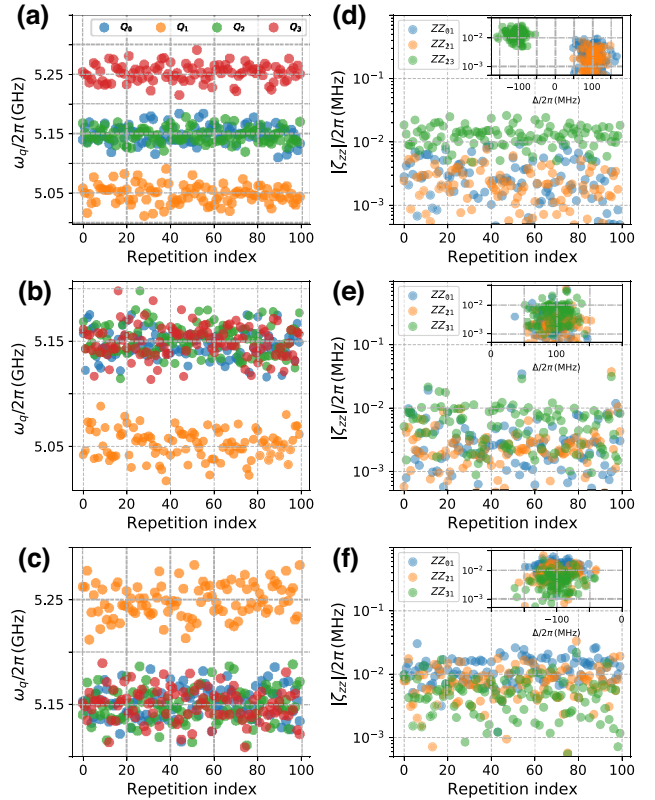


FIG. 10. Qubit frequencies and ZZ couplings of 100 repetitions. The control and target qubit frequencies are randomly distributed around their designed values, i.e., the control frequency $\omega_j/2\pi = 5.15$ GHz and the target frequency $\omega_{i(k)}/2\pi = 5.25$ (5.05) GHz, with the standard deviation of 15 MHz. (a)–(c) The qubit frequencies of 100 repetitions for the three four-qubit systems shown in Figs. 5(a)–5(c); (d)–(f) the associated ZZ couplings. Here, the other parameters are the same as in Fig. 6. The insets show the distributions of the ZZ coupling over the control-target detunings.

also show the distributions of the ZZ coupling over the control-target detunings. We find that these “exceptional” points arise mainly from static frequency collisions due to interactions between next-nearest-neighbor control qubits.

To be more specific, similar to the frequency collision of (S1) mentioned in Sec. II A 3, when the control qubit is on-resonance with its neighboring control qubit, the strong state hybridization due to the next-nearest-neighbor couplings can degrade qubit addressability and result in prominent quantum crosstalk. This is reasonable, as the frequencies of all the control qubits are distributed around the same value, making them more prone to this frequency-collision issue. For instance, in Fig. 10(e), the maximum ZZ coupling of 38 kHz is caused by the nearly on-resonance coupling of neighboring control qubits Q_2 and Q_3 . By excluding these “exceptional” points arising from these static collisions, we find that the typical ZZ coupling could be below 20 kHz. Similar to the deterioration of ZZ suppression, as we will show, such collisions can also limit the CX gate performance and cause spikes of gate errors appearing in pairs.

2. Isolated CX gates

The “violin” plots in Fig. 11 show the distributions of isolated CX gate errors with varying gate lengths. Similar to isolated two-qubit systems (see Fig. 4), here the median gate errors (indicated by dashed lines) are reduced by increasing the gate length, and the typical gate error ranges from 10^{-4} to 10^{-3} . Moreover, as shown in the insets of Fig. 11, when increasing the gate lengths, almost all qubits show decreasing trends in gate errors, suggesting that the gate error mainly comes from the CR drive. Besides, three main types of features deserve to be discussed in more detail.

(i) As shown, for example, in Fig. 11(a), under the positive detuning condition, large gate errors can be found near the detunings of 50 and 150 MHz. Following the discussion in Sec. II A, here the gate error is mainly dominated by the off-resonance transitions, i.e., the transition $|0\rangle \leftrightarrow |1\rangle$ and the two-photon transition $|0\rangle \leftrightarrow |2\rangle$ of the control qubit, which correspond to the frequency collisions (S1) and (D1). As expected, prolonging the gate length (i.e., decreasing the drive amplitude) or increasing ramp time (i.e., mitigating nonadiabatic transitions in the dressed

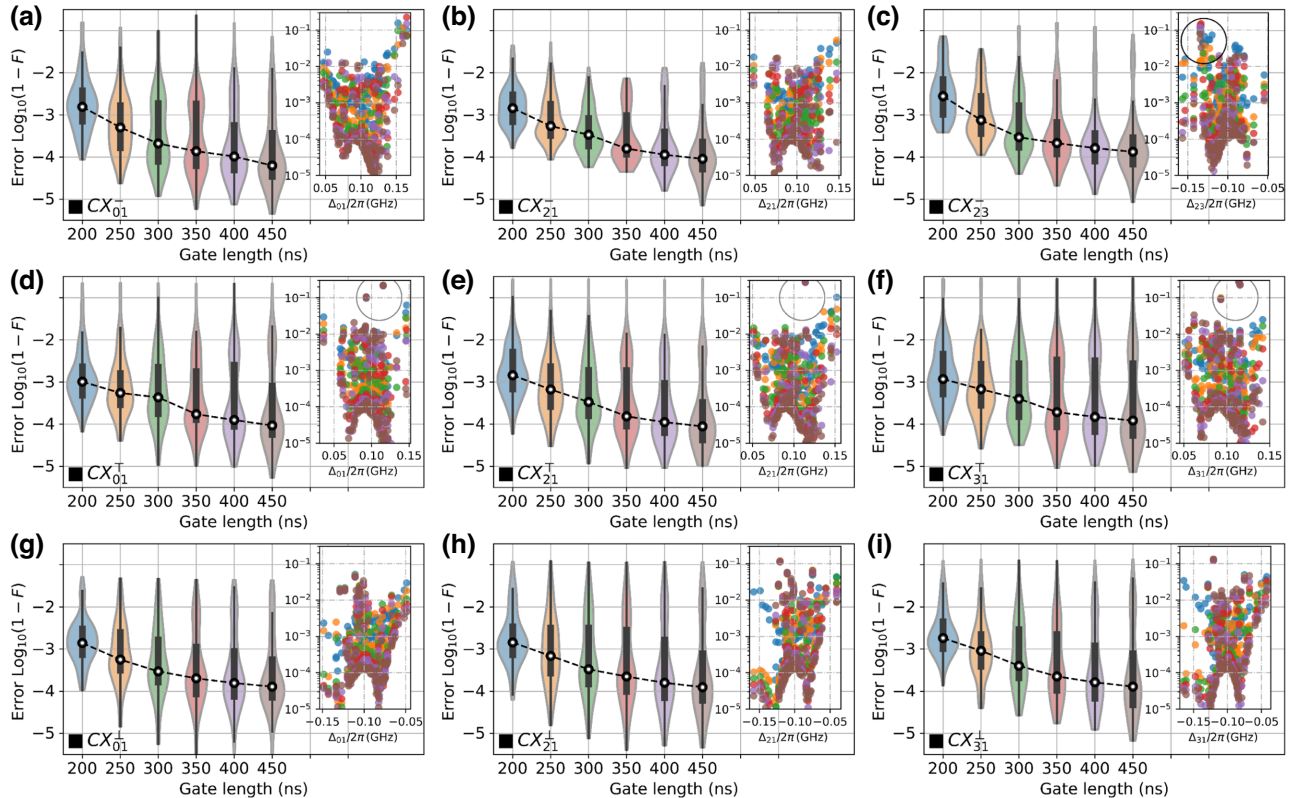


FIG. 11. Isolated CX gate errors versus gate lengths of 100 repetitions. Here, the used parameters are the same as in Fig. 10. The “violin” plots in (a)–(c), (d)–(f), and (g)–(i) show the distributions of isolated gate errors versus gate lengths for the four-qubit systems shown in Figs. 5(a), 5(b), and 5(c), respectively. The dashed lines denote the median gate error as a function of the gate length, and the insets give the error distributions over the control-target detunings. The black (gray) circles highlight the spikes of gate errors arising from frequency-collision issues.

picture, as discussed in Sec. III A), these transitions can be suppressed. Furthermore, as already discussed in previous works [51,65], we expect that off-resonance errors shown in Fig. 11 can be largely suppressed by optimizing the control pulse shape in Eq. (20).

In addition, as shown in Figs. 11(g)–11(i), under the negative detuning conditions, large gate errors can also be found near the detunings of 50 MHz. Similar to that within positive detuning conditions, this arises from the transition $|0\rangle \leftrightarrow |1\rangle$ related to the frequency collision (S1). Meanwhile, in contrast, as here the control-target detuning is negative, the two-photon transition $|0\rangle \leftrightarrow |2\rangle$ is significantly suppressed by the large detuning of ~ 265 MHz. Thus, with the negative detuning condition, the frequency-collision issue of (D1) can be safely omitted for ensuing high-fidelity gates.

(ii) Similar to the prominent ZZ crosstalk, indeed, the static collision arising from on-resonance coupling of neighboring control qubits can account for the spikes of gate errors appearing in pairs, as highlighted, for example, by the gray circles in Figs. 11(d)–11(f). More importantly, different from the dynamic collisions and the static collision discussed in Figs. 6 and 7, the current collision is almost independent of the CR drive, explaining why the resulting gate errors are not reduced by increasing the gate length, as shown in Figs. 11(d)–11(f). More specifically, Fig. 12(a) shows the CX gate errors versus the detuning between neighboring control qubits with different gate

lengths for a subsystem (consisting of Q_0 , Q_1 , and Q_2) of the “T” shape qubit system. One can find that, when the two control qubits are on-resonance, the spikes of gate errors appear in pairs (see the left and right panels) and peak values are almost independent of the gate length. Additionally, it is also shown that, since the typical coupling strength between neighboring control qubits is of the order of 50 kHz (see Sec. III A), a small detuning from the frequency collision, i.e., ~ 0.5 (2.0) MHz, is adequate to ensure gate error of ~ 0.01 (0.001).

Besides, as one might expect, the on-resonance coupling of control qubits can lead to worsening qubit addressability and will inevitably complicate almost all qubit operations (such as qubit readout), not only restricted to gate operations. It is in this sense that we argue that this type of static frequency collision deserves to be addressed with a high priority. In the current CR architecture, to avoid such static collision, one possible approach is by adding an additional always-ON off-resonant drive to selectively shift qubits [41,55]. As shown in Fig. 12(b), by applying a Stark drive to Q_0 with the detuning of 50 MHz, ensuring gate errors of 0.001 only requires an amplitude of ~ 15 MHz. As shown in the inset of Fig. 12(b), this drive induces a frequency shift of ~ 1.9 MHz, agreeing well with the estimated collision bound [see Fig. 12(a)]. Additionally, as already studied in the previous work [55], the Stark drive itself could also introduce additional error sources; this can explain why generally the performance of CX_{01}^T is worse than that of CX_{21}^T , as shown in Fig. 12(b). Moreover, with the mitigation of the frequency-collision issue, the qubit addressability could be improved and high-fidelity readout could also be possible, even under the always-ON off-resonance drive [10,72]. Similarly, as shown in Figs. 11(g)–11(i), such static collision issues also exist for the “ \perp ” shape system, and, in Appendix D, we also show the results for addressing this issue based on the ac-Stark effect.

(iii) Compared to other existing CR architectures listed in Table I, the most peculiar feature of the currently studied architecture is that the magnitude of the qubit-resonator detuning is comparable to that of the control-target detuning, as well as that of the qubit anharmonicity. This can raise a crucial question, whether this setting will introduce an additional leakage channel or error source. To answer that question, similar to the discussion of frequency collision for qubits given in Sec. II A, it should be necessary to analyze the frequency-collision issue associated with both the qubits and the resonators, which could potentially cause leakage and gate errors. Since the typical detuning between the qubit and its resonator coupler is larger than 250 MHz, frequency collisions similar to that given in Sec. II A, i.e., (S1) and (S2) and (D1) to (D4), can be ignored for the present purpose. Moreover, as it is generally assumed that all the resonator couplers are initialized in their ground states, the frequency collision should be

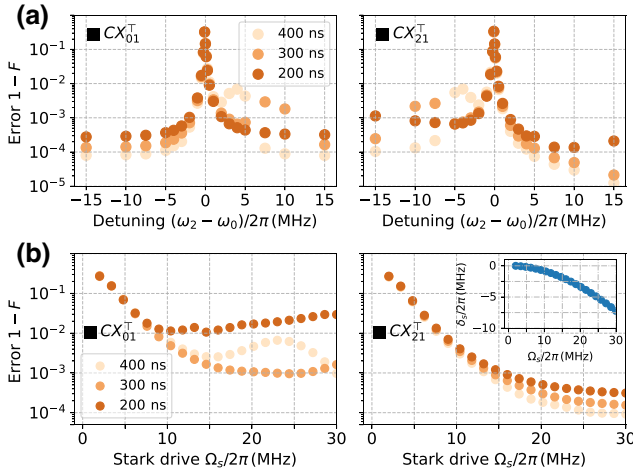


FIG. 12. (a) CX gate errors versus the detuning between neighboring control qubits (Q_0 and Q_2) with different gate lengths for a three-qubit subsystem of the “T” shape system. Here, the qubit frequencies of Q_0 and Q_1 are 5.15 and 5.05 GHz, respectively, and the other parameters are the same as in Figs. 11(d) and 11(e). (b) CX gate errors with the presence of an always-ON off-resonance drive applied to Q_0 . Here, the frequency of Q_2 is 5.15 GHz and the Stark drive frequency is 5.20 GHz. The inset shows the ac-Stark shift δ_s versus the drive amplitude Ω_s .

enabled by the CR drive-induced multiphoton process, thus acting as a dynamic one.

Accordingly, considering the present frequency setting (i.e., $\omega_i > \omega_j > \omega_k$) and the typical parameters listed in Table II, we can expect that the leading frequency collision should satisfy the following relation D_r (see Appendix E for details):

$$\omega_r + \omega_j = 2\omega_i. \quad (23)$$

This describes the two-photon transition $|0000\rangle \leftrightarrow |1100\rangle$ in the coupled qubit-resonator system, wherein the state is denoted by $|R_1, Q_j, R_2, Q_i\rangle$, and the transition rate can be approximated by (applying second-order perturbation theory) [48,73,74]

$$V_{00\leftrightarrow 11} \simeq \frac{2g_{rq}\Omega^2\alpha_q}{(\alpha_q + \Delta_q)\Delta_q^2}. \quad (24)$$

Similarly, the two-photon transition $|0100\rangle \leftrightarrow |1200\rangle$ with the condition $\omega_r + \omega_j + \alpha_j = 2\omega_i$ can occur, but the transition is heavily suppressed by the large qubit-resonator detuning Δ_{rq} and the negative anharmonicity of transmons in our setting [60] (see Appendix E for details).

Indeed, the dynamic frequency collision D_r causes the spikes of gate errors highlighted by the black circle in the inset of Fig. 11(c). To provide a more detailed analysis of the collision issue, Fig. 13(a) shows the gate errors as a function of Q_3 for a subsystem (consisting of Q_1 , Q_2 , and Q_3) of the “-” shape qubit system. As expected [see Eq. (E3)], the presence of this dynamic collision does not

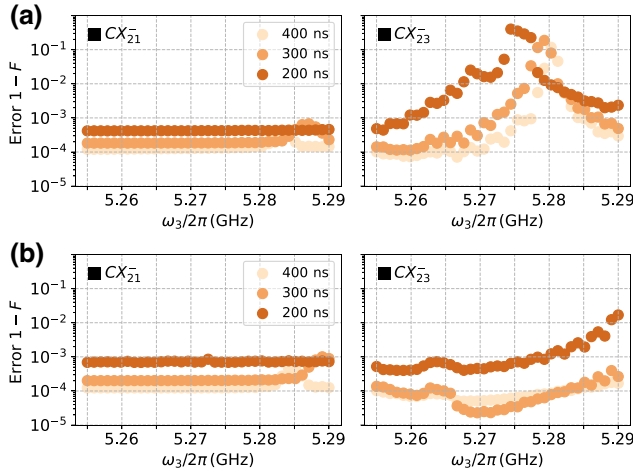


FIG. 13. (a) CX gate errors as a function of the frequency of Q_3 with different gate lengths for a three-qubit subsystem of the “-” shape system. Here, the qubit frequencies of Q_1 and Q_2 are 5.05 and 5.15 GHz, respectively, and the other parameters are the same as in Fig. 11(c). (b) CX gate errors with increased frequency of the lightweight resonator. Here, the frequency of resonator R_1 is 5.45 GHz.

affect the performance of CX_{21}^- while it can significantly degrade the CX_{23}^- gate performance. Moreover, it also illustrates the typical features of dynamic frequency collisions, i.e., both the collision condition and the induced gate error (transition rate) show a dependence on the CR drive amplitude (gate length). This suggests that, to avoid the detrimental impact of such collision, one can optimize the gate length, similar to the case discussed in Fig. 6. Besides, according to Eq. (E3), increasing the resonator frequency can be an alternative approach for this purpose, as shown in Fig. 13(b), which shows the CX gate errors with a larger resonator frequency. Additionally, in Appendix D, we also show that such collisions can also be mitigated through the ac-Stark shift, similar to the one illustrated in Fig. 12(b).

3. Simultaneous CX gates

Here, we turn to study CX gates implemented in parallel, especially focusing on simultaneous CX gates in the “-” shape four-qubit system shown in Fig. 5(a). In Fig. 14(a), the violin plot shows the distributions of simultaneous gate errors $1 - F_{\text{simul}}$ versus the gate length. Similar to that shown in Fig. 9, the median gate errors (indicated by dashed lines) decrease when increasing the gate length,

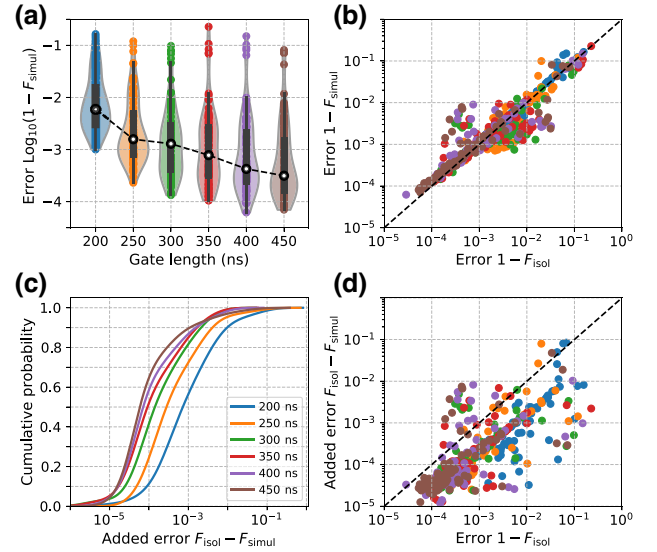


FIG. 14. Gate errors of the simultaneous CX gates ($CX_{01}^- \otimes CX_{23}^-$) in the “-” shape four-qubit system versus gate lengths of 100 repetitions. Here, the parameters used are the same as in Figs. 11(a) and 11(c). (a) Violin plot of the distributions of simultaneous gate errors ($1 - F_{\text{simul}}$) versus gate lengths. The dashed line denotes the median gate error as a function of the gate length. (b) Scatter plot of the distributions of simultaneous gate errors over the isolated errors. Here, the isolated error is obtained by adding the errors of the constituent isolated gates in Figs. 11(a) and 11(c). (c) Cumulative distribution of the added gate errors $F_{\text{isol}} - F_{\text{simul}}$ (excluding negative values, see text). (d) Scatter plot of the distributions of the added gate errors over the isolated errors.

in line with the expectation that the dominant gate error comes from the CR drive. Moreover, the simultaneous gate errors show a clear linear dependence on the isolated gate errors, as shown in Fig. 14(b).

Besides, a close look at Fig. 14(b) also shows us that, while the simultaneous gate performance is generally worse than that of the isolated one, in some cases (especially for isolated gates with the fidelities limited by leakage), the simultaneous gate can show better performance. As already noted in the previous work [60], here the isolated gates are characterized by assuming spectator qubits in ground states. Thus leakage that occurs during isolated gate operations (such as, see Fig. 6, when qubits are on-resonance with spectator qubits) will contribute to the control error of simultaneous gates. In this sense, the presence of such a situation is partly due to our ill-defined metric and thus the added error is only indicative. Excluding such cases, Fig. 14(c) shows the cumulative distribution of the added gate errors $F_{\text{isol}} - F_{\text{simul}}$. It is shown that the median added error is below 10^{-3} and can further reduce by increasing the gate length. For instance, with a gate length of 350 ns, the median error can be suppressed below 10^{-4} .

To further evaluate the effect of quantum crosstalk residing in the currently studied architecture, in Fig. 14(d) we also show the distributions of added errors over the isolated gate errors. One can see that, in almost all the cases, the added errors are smaller than that of the associated isolated gates. This suggests that, in the currently studied architecture, there exists no additional quantum crosstalk that contributes significantly to gate errors for CX gates implemented in parallel.

IV. DISCUSSION

In this section, we briefly summarize the main frequency-collision issue in the currently studied CR architecture and give potential approaches to address this issue. Then, we provide a discussion of parameter sensitivity in the current architecture.

A. Revisiting the frequency-collision issue

As discussed in Secs. II A and III, according to the underlying mechanism, the frequency collision can be classified into two main types, static and dynamic. Accordingly, near frequency-collision regions, the two types of collisions can be described by the following effective two-level Hamiltonian given in the dressed state picture (see Fig. 8):

$$H_{\text{sc}} = \frac{\delta_{s0} + \delta_s(\Omega)}{2}Z + \frac{\lambda_s}{2}X, \quad (25)$$

$$H_{\text{dc}} = \frac{\delta_{d0} + \delta_d(\Omega)}{2}Z + \frac{\lambda_d(\Omega)}{2}X, \quad (26)$$

where H_{sc} and H_{dc} are for describing the static and the dynamic collisions, respectively. Here, δ_{s0} (δ_{d0}) denotes the two-level detuning without the CR drive, while $\delta_s(\Omega)$ ($\delta_d(\Omega)$) is the ac-Stark shift, generally displaying a quadratic dependence on the drive amplitude Ω [see Eq. (22)]; λ_s denotes the coupling enabling the static collisions and is almost independent of the drive amplitude, while $\lambda_d(\Omega)$ is the coupling for the dynamic collision and strongly depends on the CR drive amplitude. Below, based on Eqs. (25) and (26), we give more detailed discussions on the frequency collision.

(i) *Static frequency collision.* As in Eq. (25), the static collision and the associated frequency bound mainly depend on the static couplings λ_s , such as couplings between near-neighbors or beyond. To mitigate such collisions, a finite detuning of δ_{s0} should be retained with the highest priority. Otherwise, this will worsen qubit addressability and significantly complicate almost all of the qubit operations. On the other hand, even with the predefined detuning δ_{s0} , the CR drive can shift qubits, giving rise to the additional detuning $\delta_s(\Omega)$. This means that the on-resonance condition can be achieved at specific drive amplitudes, as shown in Figs. 6 and 7. Thus, to further avoid such situations, the drive amplitude (gate length) should be optimized, keeping away from the on-resonance point (see Figs. 6 and 7). In the currently studied CR architecture, the collision issue for neighboring qubits can be largely mitigated by using the three-frequency allocation scheme on the heavy-hexagonal qubit lattice, as illustrated in Figs. 1(a) and 1(e). However, given the three-frequency pattern, neighboring control qubits are prone to such collision issues. Hopefully, the typical coupling is at the submegahertz level, thus, according to Eq. (25), a small detuning is adequate for addressing such issues [see Fig. 12(a)]. Meanwhile, even without the predefined detuning δ_{s0} , adding a weak off-resonant drive to selectively shift qubits can mitigate this issue, as demonstrated in Fig. 12(b).

(ii) *Dynamic frequency collision.* From Eq. (26), both the detuning and the coupling depend on the CR drive amplitude [69]. In essence, this issue is generally manifested as drive-induced single- or multiphoton transitions, which are absent when the drive is turned off, and the main types are summarized in Sec. II A. Accordingly, both the resulting gate error and the occurrence condition can show a clear dependence on the drive amplitude, as shown, for example, in Fig. 13(a). Thus, generally, to mitigate the issue, one can keep a predefined detuning δ_{d0} and decrease the drive amplitude. On the other hand, besides improving the accuracy in setting δ_{d0} , one might prefer to optimize the control pulse for ensuring fast gates [51,65]. In the dressed state picture, this corresponds to suppressing the nonadiabatic transitions which are dominated by the collisions with large couplings. Note that, similar to baseband flux-control gate operations [60], in the long term, one should

balance gate errors due to frequency collisions with small couplings (submegahertz, favoring fast gates) and with large couplings (few megahertz, preferring slow gates).

In the present architecture based on the heavy-hexagonal layout and the allocation scheme shown in Figs. 1(a) and 1(e), the dynamics collision issue for neighboring qubits can be largely mitigated by assuming the state-of-the-art accuracy in setting qubit frequencies [24], as shown in Fig. 10. But, indeed, new frequency collisions can be introduced here, as indicated by Eq. (E3), due to the small qubit-resonator detuning (note that, as shown in Fig. 2(c), within the architecture with the multipath coupler, this issue should be heavily suppressed). In Fig. 13(b), we show that increasing the resonator frequency, i.e., increasing δ_{d0} in Eq. (26), can address this issue while it does not seriously affect the gate speed [see also Fig. 4(a)]. Additionally, as illustrated in Appendix D, this issue can also be mitigated by adding off-resonance drives. Note that, unlike the static collision, here the dynamics collision is activated by the CR drive. Thus, in principle, the off-resonance drive could only be applied during gate operations [55,56], rather than being applied in an always-ON manner. In this scenario, to ensure high-fidelity state maps between the computational basis and microwave-dressed basis, the Stark drive should be slowly ramped up or down [55].

B. Parameter sensitivity

As illustrated in Secs. II and III, in the currently studied architecture, the realization of fast CR gates with ZZ suppression depends strongly on the accuracy in setting qubit parameters. For instance, assuming the control-target detuning of 100 MHz and the ZZ coupling suppressed below 10 kHz, the typical usable range of qubit-resonator detuning for ensuring fast gates (here we consider that, assuming a CR drive amplitude of 50 MHz, the target ZX rate is 1 MHz) is only about 100 MHz, as shown in Figs. 2(d) and 3. Considering the fabrication uncertainty, within the current architecture, ensuring the successful realization of fast gates with ZZ suppression should be a nontrivial task.

Generally, there are two kinds of solutions for this issue: (i) Optimizing system parameters. For instance, by increasing the qubit-resonator coupling, the useful regime can increase to ~ 200 MHz with the ZZ coupling suppressed below 20 kHz (see the figure in Appendix B). In addition, decreasing the control-target detuning could be an alternative approach, but, to ensure high-fidelity gates, the detuning should be far away from the on-resonance condition (S1). (ii) Adjusting qubit or resonator parameters after fabrication. For example, similar to the mitigation of the frequency-collision issue, this issue can be largely addressed by improving the precision in setting qubit frequencies with laser-annealing techniques [24,75].

Besides, given that the frequency reproducibility of resonators can be far better than that of qubits (see, e.g., Ref. [66]), the qubit and the resonator coupler could be placed in separate chips within flip-chip architectures. As a consequence, each qubit can have its dedicated resonator coupler for realizing a fast gate with ZZ suppression.

V. CONCLUSION

We introduce a CR architecture based on fixed-frequency transmons and fixed qubit-qubit couplings for mitigating both quantum crosstalk and frequency-collision issues. Within the CR architecture, we show that the proposed lightweight resonator coupler allows us to address the speed-fidelity trade-off issue imposed by quantum crosstalk and extend the usable operating region with sizable ZX couplings. Given typical qubit parameters, we demonstrate, both analytically and numerically, that ZZ quantum crosstalk can be suppressed and fast, high-fidelity CR gates can also be achieved with the condition of negative control-target detunings.

Accordingly, we move beyond the existing literature by operating the qubit system at both the positive and negative detuning regions. This could largely mitigate the frequency-collision issue in existing architectures. To assess the feasibility and utility, assuming the state-of-the-art precision in setting frequencies, we systematically analyze the CX gate performance in the proposed architecture and show that quantum crosstalk and frequency-collision issues can be largely mitigated, while the remaining collision issue can be addressed by adding weak off-resonance drives. This suggests that the architecture proposed here could be feasible, even considering practical challenges, especially fabrication uncertainties.

Although here we mainly focus on the heavy-hexagonal layout, one can reasonably expect that, within the introduced CR architecture, the quantum crosstalk and the frequency-collision issues in square qubit lattices can also be suppressed. However, as studied in previous works [24,33], to avoid frequency collisions and to improve the fabrication yield, more stringent requirements, especially in setting the qubit frequency, would be required for the square layout than for the heavy-hexagonal layout.

To further improve gate performance and mitigate frequency collisions, we give an intuitive model based on the dressed state picture. Accordingly, we illustrate the general underlying mechanism of frequency collisions and show that frequency collisions can be classified into two main types, i.e., static and dynamic. We further provide dedicated schemes to mitigate the two types of frequency collisions. While the analysis focuses on the CR architecture with transmon qubits, we expect that these discussions could also be useful for other qubit architecture with all-microwave-activated gate operations [40,41,53,73].

Supporting long coherence times and low control overhead while protecting the qubit system from quantum crosstalk effects should be one of the most crucial steps toward large-scale quantum processors based on fixed-frequency qubits and fixed couplings. The present work could be helpful in guiding the design of CR-gate-based architectures for this purpose.

ACKNOWLEDGMENTS

The author would like to thank Pei Liu, Yingshan Zhang, and Ziting Wang for many helpful discussions on the CR-gate-based transmon architecture. Thanks also go to Meng-Jun Hu, Zhikun Han, and Fei Yan for their insightful comments, especially about the time stability of qubit performance in superconducting quantum processors. The author would also like to thank Guangming Xue, Peng Xu, and Haifeng Yu for their generous support and encouragement. The author gratefully acknowledges support from the National Natural Science Foundation of China (Grant No. 12204050) and the Beijing Academy of Quantum Information Sciences.

APPENDIX A: PARASITIC INTERACTIONS AND THEIR IMPACT ON THE CR ARCHITECTURE

As mentioned in Sec. II A, stray couplings between qubits are ubiquitous in real superconducting qubit devices. Here, we turn to provide specific cases for illustrating their effects on ZZ suppression and ZX rates. As mentioned in the second column of Table I, we consider a

direct qubit-qubit coupling arising from an effective capacitance [34,57], giving rise to $g_{12} = 2g_{r1}g_{r2}/\omega_r$. By including such direct qubit-qubit coupling terms, we go back to the generalized system model described by the Hamiltonian in Eq. (1). Following Eqs. (6), (12), and (17), in Fig. 15, we show the ZZ coupling, XY coupling, and the ZX rate as functions of the resonator frequency with different qubit-resonator couplings. Here, the used parameters are the same as in Fig. 3.

It is shown that, considering the direct couplings, suppressing ZZ couplings and maintaining ZX couplings with sizable strengths can still be achieved. While, for the given qubit-resonator coupling, both the XY (ZZ) coupling and the ZX rate strength are reduced compared to that without taking into account the stray coupling [see Figs. 15(a) and 3], increasing the qubit-resonator coupling here should be a practical solution to such concern, as shown in Fig. 15(b). Moreover, the usable frequency range is comparable to that shown in Fig. 3.

APPENDIX B: EFFECT OF THE INCREASED QUBIT-BUS COUPLING ON THE CR ARCHITECTURE

Within the proposed CR architecture, as mentioned in Sec. II B, increasing the qubit-resonator coupling could be a practical solution to further improve the ZX rate, as well as the usable parameter range. Meanwhile, this can also give rise to larger ZZ couplings. Figure 16 shows the effective interqubit couplings (ZZ and XY couplings)

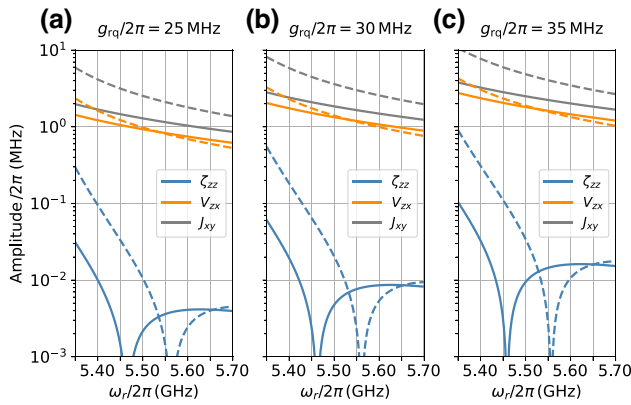


FIG. 15. Effective interqubit couplings (ZZ and XY couplings) and ZX rates versus the resonator frequency under the consideration of stray qubit-qubit couplings. Here, we consider the direct qubit-qubit coupling with the strength of $g_{12} = 2g_{r1}g_{r2}/\omega_r$. In panels (a), (b), and (c), the strengths of the qubit-resonator couplings are 25, 30, and 35 MHz, respectively. The other used parameters are the same as in Fig. 3. The solid and dashed lines denote the results for the system with positive and negative control-target detunings, respectively.

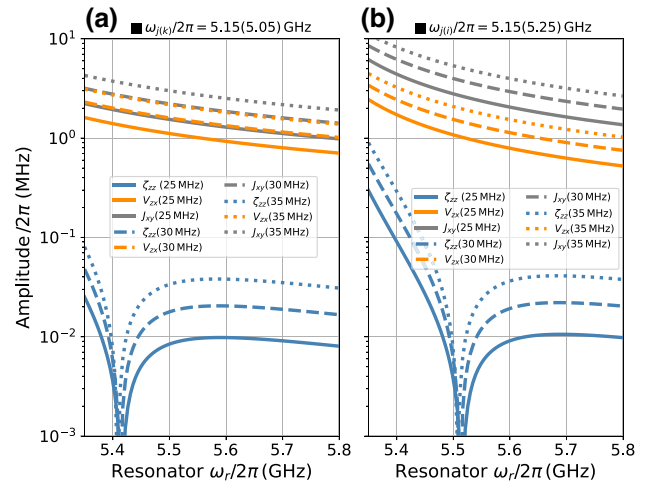


FIG. 16. Effective interqubit couplings (ZZ and XY couplings) and ZX rates versus the resonator frequency with different qubit-resonator couplings. (a) Positive control-target detunings. (b) Negative control-target detunings. The solid, dashed, and dotted lines denote the results with the qubit-resonator couplings of 25, 30, and 35 MHz, respectively. The other used parameters are the same as in Fig. 3.

and ZX rates versus the resonator frequency with different qubit-resonator couplings. It is shown that, when increasing the qubit-resonator coupling, both the ZX rate and the useful range of the qubit-resonator detuning can also be enhanced. However, for instance, increasing the qubit-resonator coupling from 25 to 30 (35) MHz, accordingly, will increase the typical ZZ coupling from 10 to 20 (40) kHz. On the other hand, similar to the multipath coupler [42,43], even in these cases, the typical magnitude of J_{xy}/ζ_{zz} can still reach the order of 10^2 , suggesting that the proposed architecture can still outperform other existing architectures, such as architectures with capacitor couplers or resonator couplers [see Figs. 2(a) and 2(b)].

APPENDIX C: THE TUNE-UP PROCEDURE AND CHARACTERIZATION OF THE DIRECT CX GATE

In the present work, we consider the implementation of the direct CX gate by simultaneously driving both the control qubit Q_1 and the target qubit Q_2 , as described by the drive Hamiltonian given in Eq. (19). As mentioned in Sec. II B, the used pulse shape is a cosine-decorated square pulse with fixed ramp times of 20 ns, given in Eq. (20). For tuning up CX gates with a fixed gate length of t_g , we consider numerically optimizing the two drive amplitudes $\{\Omega_1, \Omega_2\}$, which are the peak drive amplitudes of the two applied drives [see Eq. (20)], and the used loss function is defined as

$$L(\Omega_1, \Omega_2) = \langle N_{00,01} \rangle + \langle 1 - N_{10,11} \rangle, \quad (\text{C1})$$

where $N_{00,01}$ ($N_{10,11}$) denotes the population in state $|00\rangle$ ($|10\rangle$) after the gate operation with the system initialized in state $|000\rangle$ ($|100\rangle$). Here, $|nml\rangle$ denotes the eigenstate of the static Hamiltonian in Eq. (14), which is adiabatically connected to the bare state $|nml\rangle$. The first term in Eq. (C1) has the effect of minimizing the excitation of Q_2 when Q_1 is in state $|0\rangle$, while the second term is for ensuring a complete flip of Q_2 when Q_1 is in state $|1\rangle$.

After obtaining the optimal drive amplitudes $\{\Omega_1, \Omega_2\}$, according to the full system Hamiltonian [see Eqs. (14) and (19)],

$$H_{\text{full}} = H_{\text{static}} + H_{\text{drive}}, \quad (\text{C2})$$

and the pulse shape given in Eq. (20), the actual evolution operator is given by

$$U = \hat{T} \exp \left(-i \int_0^{t_g} H_{\text{full}}(t) dt \right), \quad (\text{C3})$$

where \hat{T} denotes the time-ordering operator. Up to single-qubit Z phases, the gate fidelity of the implemented CX gate

is [62]

$$F = \frac{\text{Tr}(\tilde{U}^\dagger \tilde{U}) + |\text{Tr}(U_{\text{CX}}^\dagger \tilde{U})|^2}{20}, \quad (\text{C4})$$

where \tilde{U} denotes the actual evolution operator, which is truncated to the two-qubit computational subspace spanned by $\{|000\rangle, |001\rangle, |100\rangle, |101\rangle\}$, and U_{CX} denotes the target CX gate:

$$U_{\text{CX}} = \begin{pmatrix} 1 & 0 & 0 & 0 \\ 0 & 1 & 0 & 0 \\ 0 & 0 & 0 & 1 \\ 0 & 0 & 1 & 0 \end{pmatrix}. \quad (\text{C5})$$

In our analysis of the CX gate performance, the above procedure is applied to both the isolated two-qubit system shown in Fig. 4 and the four-qubit systems shown in Fig. 5. Additionally, for tuning up and characterizing an isolated CX gate in the multiqubit system, we always assume that all the spectator qubits are in their ground states. Then, the simultaneous gates are characterized based on the pulse parameters obtained from the tune-up procedure of the constituent isolated gates. Lastly, note here that, in our numerical analysis, each transmon qubit is modeled as a four-level anharmonic oscillator and the resonator is truncated to the lowest four energy levels.

APPENDIX D: MITIGATING THE FREQUENCY-COLLISION ISSUE WITH THE ac-STARK SHIFT

As illustrated in Sec. III B, the static collision arising from weak qubit-qubit couplings can be avoided by adding weak off-resonance Stark drives. Here, we provide additional illustrations on this subject. Similar to Fig. 12(a), Fig. 17(a) shows that the static collision arising from the always-ON weak coupling between neighboring control qubits Q_0 and Q_2 can also exist for systems with negative control-target detunings. By applying an off-resonance drive to Q_0 at the frequency of 5.20 GHz, this collision issue can also be mitigated by employing the ac-Stark effect [see Fig. 17(b)].

In addition, while in Sec. III B, the dynamic collision issue associated with the resonator is addressed at the device level, i.e., by increasing the resonator frequency, here we further show that this issue can also be mitigated by adding off-resonance drive to selectively shift qubit frequencies. Accordingly, Fig. 18 shows the CX gate performance in the subsystem (comprising Q_1 , Q_2 , and Q_3) of the “—” shape four-qubit system with the off-resonance drive applied to Q_3 . It is shown that the gate performance can indeed be improved. By optimizing the gate length and the Stark drive parameters, we expect that even higher gate fidelities can be achieved.

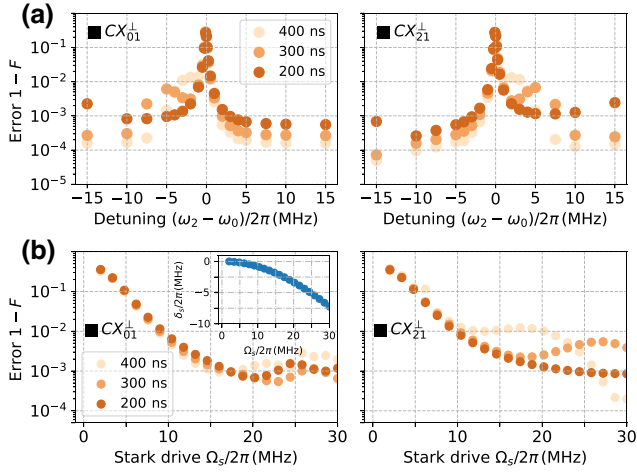


FIG. 17. (a) CX gate errors versus the detuning between neighboring control qubits (Q_0 and Q_2) with different gate lengths for the subsystem of the “ \perp ” shape system. Here, the qubit frequencies of Q_0 and Q_1 are 5.15 and 5.25 GHz, respectively. The other parameters are the same as in Figs. 11(g) and 11(h). (b) CX gate errors with the presence of an always-ON off-resonance drive applied to Q_0 . Here, the frequency of Q_2 is 5.25 GHz and the Stark drive frequency is 5.20 GHz. The inset shows the ac-Stark shift δ_s versus the drive amplitude Ω_s .

Note here that, besides two-qubit gates, the impact of the introduced off-resonance drive on single-qubit gates should also be examined. As demonstrated theoretically in the previous work [55], even in the presence of off-resonance drives, single-qubit gates with gate errors below 0.0001 could still be achieved, especially when using a small drive amplitude, as in the present work.

APPENDIX E: NEWLY ADDED FREQUENCY COLLISIONS

Within the currently studied architecture, the magnitude of the qubit-resonator detuning is comparable to that

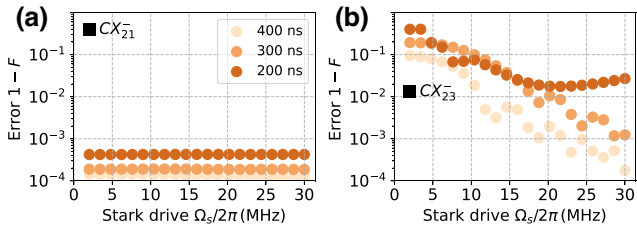


FIG. 18. CX gate errors versus the Stark drive amplitude with different gate lengths for the subsystem of the “ $-$ ” shape system. Here, the qubit frequencies of Q_1 and Q_2 are 5.05 and 5.15 GHz, respectively, while the frequency of Q_3 is 5.28, 5.279, and 5.2745 GHz for gate lengths of 400, 300, and 200 ns, respectively (as here the collision condition depends on the drive amplitude). The Stark drive is applied to Q_3 at a frequency of 5.33 GHz and the other parameters are the same as in Fig. 11(c).

of the control-target detuning and the qubit anharmonicity. This can thus introduce new frequency-collision issues associated with both the qubits and the resonators. Moreover, since the resonator frequency is larger than the qubit frequency, with the typical detuning of 250 MHz, frequency-collision issues similar to (S1), (S2), and (D1) to (D4) (see Sec. II A) can be ignored here. Considering that the resonator couplers are generally initialized in their ground states, the leading frequency collision should be manifested as CR-drive-induced two-photon transitions.

To be more specific, we consider a coupled qubit-resonator system, wherein $\Delta_q = \omega_q - \omega_r$ and g_{rq} denote the qubit-resonator detuning and the qubit-resonator coupling, respectively, and the system state is labeled by $|Q, R\rangle$. We further assume that a drive with frequency ω_d and drive magnitude Ω is applied to the qubit, which is a transmon qubit with anharmonicity α_q . Within such a coupled qubit-resonator system, there are two main types of two-photon transitions with the resonance conditions

$$\begin{aligned} \omega_r + \omega_q &= 2\omega_d, \\ \omega_r + \omega_q + \alpha_q &= 2\omega_d, \end{aligned} \quad (\text{E1})$$

which correspond to the two-photon transitions $|00\rangle \leftrightarrow |11\rangle$ and $|10\rangle \leftrightarrow |21\rangle$, respectively. By applying second-order perturbation theory [48,73], the transition rate can be approximated by

$$\begin{aligned} V_{00 \leftrightarrow 11} &\simeq \frac{2g_{rq}\Omega^2\alpha_q}{(\alpha_q + \Delta_q)\Delta_q^2}, \\ V_{10 \leftrightarrow 21} &\simeq \frac{-\sqrt{2}\Omega}{\Delta_q + \alpha_q} \left[\frac{-4g_{rq}\Omega}{\Delta_q + \alpha_q} + \frac{g_{rq}\Omega}{\Delta_q} + \frac{3g_{rq}\Omega}{\Delta_q + 2\alpha_q} \right]. \end{aligned} \quad (\text{E2})$$

As mentioned in Sec. III, considering the three-frequency setting, i.e., $\omega_i > \omega_j > \omega_k$, for the heavy-hexagonal qubit lattice and the typical parameters listed in Table II, we find that, within the currently studied CR architecture, the dominant frequency collision should be the two-photon transition $|00\rangle \leftrightarrow |11\rangle$ and the collision condition is given by

$$\omega_r + \omega_j = 2\omega_i. \quad (\text{E3})$$

On the other hand, as indicated by Eq. (E2), the two-photon transition $|10\rangle \leftrightarrow |21\rangle$ is heavily suppressed by the large qubit-resonator detuning and the negative anharmonicity of transmon qubits.

-
- [1] J. M. Martinis, Qubit metrology for building a fault tolerant quantum computer, *Npj Quantum Inf.* **1**, 15005 (2015).
 - [2] P. Krantz, M. Kjaergaard, F. Yan, T. P. Orlando, S. Gustavsson, and W. D. Oliver, A quantum engineer’s guide

- to superconducting qubits, *Appl. Phys. Rev.* **6**, 021318 (2019).
- [3] A. Blais, A. L. Grimsmo, S. M. Girvin, and A. Wallraff, Circuit quantum electrodynamics, *Rev. Mod. Phys.* **93**, 025005 (2021).
- [4] R. C. Bialczak, M. Ansmann, M. Hofheinz, M. Lenander, E. Lucero, M. Neeley, A. D. O’Connell, D. Sank, H. Wang, M. Weides, J. Wenner, T. Yamamoto, A. N. Cleland, and J. M. Martinis, Fast Tunable Coupler for Superconducting Qubits, *Phys. Rev. Lett.* **106**, 060501 (2011).
- [5] G. S. Paraoanu, Microwave-induced coupling of superconducting qubits, *Phys. Rev. B* **74**, 140504(R) (2006).
- [6] C. Rigetti and M. Devoret, Fully microwave-tunable universal gates in superconducting qubits with linear couplings and fixed transition frequencies, *Phys. Rev. B* **81**, 134507 (2010).
- [7] P. C. de Groot, J. Lisenfeld, R. N. Schouten, S. Ashhab, A. Lupaşcu, C. J. P. M. Harmans, and J. E. Mooij, Selective darkening of degenerate transitions demonstrated with two superconducting quantum bits, *Nat. Phys.* **6**, 763 (2010).
- [8] J. M. Chow, A. D. Córcoles, J. M. Gambetta, C. Rigetti, B. R. Johnson, J. A. Smolin, J. R. Rozen, G. A. Keefe, M. B. Rothwell, M. B. Ketchen, and M. Steffen, Simple All-Microwave Entangling Gate for Fixed-Frequency Superconducting Qubits, *Phys. Rev. Lett.* **107**, 080502 (2011).
- [9] J. Koch, T. M. Yu, J. Gambetta, A. A. Houck, D. I. Schuster, J. Majer, A. Blais, M. H. Devoret, S. M. Girvin, and R. J. Schoelkopf, Charge-insensitive qubit design derived from the Cooper pair box, *Phys. Rev. A* **76**, 042319 (2007).
- [10] E. H. Chen, T. J. Yoder, Y. Kim, N. Sundaresan, S. Srinivasan, M. Li, A. D. Córcoles, A. W. Cross, and M. Takita, Calibrated Decoders for Experimental Quantum Error Correction, *Phys. Rev. Lett.* **128**, 110504 (2022).
- [11] N. Sundaresan, T. J. Yoder, Y. Kim, M. Li, E. H. Chen, G. Harper, T. Thorbeck, A. W. Cross, A. D. Córcoles, and M. Takita, Demonstrating multi-round subsystem quantum error correction using matching and maximum likelihood decoders, *Nat. Commun.* **14**, 2852 (2023).
- [12] Y. Kim, A. Eddins, S. Anand, K. X. Wei, E. v. d. Berg, S. Rosenblatt, H. Nayfeh, Y. Wu, M. Zaletel, K. Temme, and A. Kandala, Evidence for the utility of quantum computing before fault tolerance, *Nature* **618**, 500-505 (2023).
- [13] P. Jurcevic *et al.*, Demonstration of quantum volume 64 on a superconducting quantum computing system, *Quantum Sci. Technol.* **6**, 025020 (2021).
- [14] J. M. Chow, J. M. Gambetta, A. D. Córcoles, S. T. Merkel, J. A. Smolin, C. Rigetti, S. Poletto, G. A. Keefe, M. B. Rothwell, J. R. Rozen, M. B. Ketchen, and M. Steffen, Universal Quantum Gate Set Approaching Fault-Tolerant Thresholds with Superconducting Qubits, *Phys. Rev. Lett.* **109**, 060501 (2012).
- [15] A. P. M. Place *et al.*, New material platform for superconducting transmon qubits with coherence times exceeding 0.3 milliseconds, *Nat. Commun.* **12**, 1779 (2021).
- [16] C. Wang *et al.*, Towards practical quantum computers: Transmon qubit with a lifetime approaching 0.5 milliseconds, *Npj Quantum Inf.* **8**, 3 (2022).
- [17] R. T. Gordon, C. E. Murray, C. Kurter, M. Sandberg, S. A. Hall, K. Balakrishnan, R. Shelby, B. Wacaser, A. A. Stabile, J. W. Sleight, M. Brink, M. B. Rothwell, K. P. Rodbell, O. Dial, and M. Steffen, Environmental radiation impact on lifetimes and quasiparticle tunneling rates of fixed-frequency transmon qubits, *Appl. Phys. Lett.* **120**, 074002 (2022).
- [18] S. Sheldon, E. Magesan, J. M. Chow, and J. M. Gambetta, Procedure for systematically tuning up cross-talk in the cross-resonance gate, *Phys. Rev. A* **93**, 060302(R) (2016).
- [19] A. D. Patterson, J. Rahamim, T. Tsunoda, P. A. Spring, S. Jebari, K. Ratter, M. Mergenthaler, G. Tancredi, B. Vlastakis, M. Esposito, and P. J. Leek, Calibration of a cross-resonance two-qubit gate between directly coupled transmons, *Phys. Rev. Appl.* **12**, 064013 (2019).
- [20] H. Paik, S. Srinivasan, S. Rosenblatt, J. Chavez-Garcia, D. Bogorin, O. Jinka, G. Keefe, D. Shao, J.-B. Yau, M. Brink, and J. M. Chow, Coupler characterization of superconducting transmons qubits for cross-resonance gate, 2020 IEEE International Electron Devices Meeting (IEDM), (2020), p. 38.2.1.
- [21] J. M. Chow, S. J. Srinivasan, E. Magesan, A. D. Córcoles, D. W. Abraham, J. M. Gambetta, and M. Steffen, Characterizing a four-qubit planar lattice for arbitrary error detection, *Proc. SPIE 9500, Quantum Inf. Comput.* **13**, 95001G (2015).
- [22] J. M. Gambetta, J. M. Chow, and M. Steffen, Building logical qubits in a superconducting quantum computing system, *Npj Quantum Inf.* **3**, 2 (2017).
- [23] M. Brink, J. M. Chow, J. Hertzberg, E. Magesan, and Sami Rosenblatt, Device challenges for near term superconducting quantum processors: Frequency collisions, 2018 IEEE International Electron Devices Meeting (IEDM), (2018).
- [24] J. B. Hertzberg, E. J. Zhang, S. Rosenblatt, E. Magesan, J. A. Smolin, J.-B. Yau, V. P. Adiga, M. Sandberg, M. Brink, Je. M. Chow, and J. S. Orcutt, Laser-annealing Josephson junctions for yielding scaled-up superconducting quantum processors, *Npj Quantum Inf.* **7**, 129 (2021).
- [25] J. M. Kreikebaum, K. P. O’Brien, A. Morvan, and I. Siddiqi, Improving wafer-scale Josephson junction resistance variation in superconducting quantum coherent circuits, *Supercond. Sci. Technol.* **33**, 06LT02 (2020).
- [26] L. DiCarlo, J. M. Chow, J. M. Gambetta, L. S. Bishop, B. R. Johnson, D. I. Schuster, J. Majer, A. Blais, L. Frunzio, S. M. Girvin, and R. J. Schoelkopf, Demonstration of two-qubit algorithms with a superconducting quantum processor, *Nature (London)* **460**, 240 (2009).
- [27] J. M. Gambetta, A. D. Córcoles, S. T. Merkel, B. R. Johnson, John A. Smolin, J. M. Chow, C. A. Ryan, C. Rigetti, S. Poletto, T. A. Ohki, M. B. Ketchen, and M. Steffen, Characterization of Addressability by Simultaneous Randomized Benchmarking, *Phys. Rev. Lett.* **109**, 240504 (2012).
- [28] D. C. McKay, S. Sheldon, J. A. Smolin, J. M. Chow, and J. M. Gambetta, Three Qubit Randomized Benchmarking, *Phys. Rev. Lett.* **122**, 200502 (2019).
- [29] M. Malekakhlagh, E. Magesan, and D. C. McKay, First-principles analysis of cross-resonance gate operation, *Phys. Rev. A* **102**, 042605 (2020).
- [30] T.-Q. Cai, X.-Y. Han, Y.-K. Wu, Y.-L. Ma, J.-H. Wang, Z.-L. Wang, H.-Y. Zhang, H.-Y. Wang, Y.-P. Song, and L.-M. Duan, Impact of Spectators on a Two-Qubit Gate in a Tunable Coupling Superconducting Circuit, *Phys. Rev. Lett.* **127**, 060505 (2021).

- [31] K. Heya, M. Malekakhlagh, S. Merkel, N. Kanazawa, and E. Pritchett, Floquet analysis of frequency collisions, [arXiv:2302.12816](https://arxiv.org/abs/2302.12816).
- [32] A. Morvan, L. Chen, J. M. Larson, D. I. Santiago, and I. Siddiqi, Optimizing frequency allocation for fixed-frequency superconducting quantum processors, *Phys. Rev. Res.* **4**, 023079 (2022).
- [33] C. Chamberland, G. Zhu, T. J. Yoder, J. B. Hertzberg, and A. W. Cross, Topological and Subsystem Codes on Low-Degree Graphs with Flag Qubits, *Phys. Rev. X* **10**, 011022 (2020).
- [34] J. Ku, X. Xu, M. Brink, D. C. McKay, J. B. Hertzberg, M. H. Ansari, and B. L. T. Plourde, Suppression of Unwanted ZZ Interactions in a Hybrid Two-Qubit System, *Phys. Rev. Lett.* **125**, 200504 (2020).
- [35] P. Zhao, P. Xu, D. Lan, J. Chu, X. Tan, H. Yu, and Y. Yu, High-Contrast ZZ Interaction Using Superconducting Qubits with Opposite-Sign Anharmonicity, *Phys. Rev. Lett.* **125**, 200503 (2020).
- [36] X. Xu and M. H. Ansari, ZZ freedom in two qubit gates, *Phys. Rev. Appl.* **15**, 064074 (2021).
- [37] J. M. Chávez-García, F. Solgun, J. B. Hertzberg, O. Jinka, M. Brink, and B. Abdo, Weakly flux-tunable superconducting qubit, *Phys. Rev. Appl.* **18**, 034057 (2022).
- [38] Xuexin Xu and M. Ansari, Parasitic-free gate: An error-protected cross-resonance switch in weakly tunable architectures, *Phys. Rev. Appl.* **19**, 024057 (2023).
- [39] N. Sundaresan, I. Lauer, E. Pritchett, E. Magesan, P. Jurcevic, and J. M. Gambetta, Reducing Unitary and Spectator Errors in Cross Resonance with Optimized Rotary Echoes, *PRX Quantum* **1**, 020318 (2020).
- [40] B. K. Mitchell, R. K. Naik, A. Morvan, A. Hashim, J. M. Kreikebaum, B. Marinelli, W. Lavrijsen, K. Nowrouzi, D. I. Santiago, and I. Siddiqi, Hardware-Efficient Microwave-Activated Tunable Coupling Between Superconducting Qubits, *Phys. Rev. Lett.* **127**, 200502 (2021).
- [41] K. X. Wei, E. Magesan, I. Lauer, S. Srinivasan, D. F. Bogorin, S. Carnevale, G. A. Keefe, Y. Kim, D. Klaus, W. Landers, N. Sundaresan, C. Wang, E. J. Zhang, M. Steffen, O. E. Dial, D. C. McKay, and A. Kandala, Hamiltonian Engineering with Multicolor Drives for Fast Entangling Gates and Quantum Crosstalk Cancellation, *Phys. Rev. Lett.* **129**, 060501 (2022).
- [42] A. Kandala, K. X. Wei, S. Srinivasan, E. Magesan, S. Carnevale, G. A. Keefe, D. Klaus, O. Dial, and D. C. McKay, Demonstration of a High-Fidelity CNOT Gate for Fixed-Frequency Transmons with Engineered ZZ Suppression, *Phys. Rev. Lett.* **127**, 130501 (2021).
- [43] P. Zhao, D. Lan, P. Xu, G. Xue, M. Blank, X. Tan, H. Yu, and Y. Yu, Suppression of static ZZ interaction in an all-transmon quantum processor, *Phys. Rev. Appl.* **16**, 024037 (2021).
- [44] M. H. Goerz, F. Motzoi, K. B. Whaley, and C. P. Koch, Charting the circuit QED design landscape using optimal control theory, *Npj Quantum Inf.* **3**, 37 (2017).
- [45] L. Jin, Implementing high-fidelity two-qubit gates in superconducting coupler architecture with novel parameter regions, [arXiv:2105.13306](https://arxiv.org/abs/2105.13306).
- [46] B. Li, T. Calarco, and F. Motzoi, Nonperturbative Analytical Diagonalization of Hamiltonians with Application to Circuit QED, *PRX Quantum* **3**, 030313 (2022).
- [47] P. Zhao, Y. Zhang, G. Xue, Y. Jin, and H. Yu, Tunable coupling of widely separated superconducting qubits: A possible application toward a modular quantum device, *Appl. Phys. Lett.* **121**, 032601 (2022).
- [48] V. Tripathi, M. Khezri, and A. N. Korotkov, Operation and intrinsic error budget of a two-qubit cross-resonance gate, *Phys. Rev. A* **100**, 012301 (2019).
- [49] M. Ware, B. R. Johnson, J. M. Gambetta, T. A. Ohki, J. M. Chow, and B. L. T. Plourde, Cross-resonance interactions between superconducting qubits with variable detuning, [arXiv:1905.11480](https://arxiv.org/abs/1905.11480).
- [50] E. Magesan and J. M. Gambetta, Effective Hamiltonian models of the cross-resonance gate, *Phys. Rev. A* **101**, 052308 (2020).
- [51] M. Malekakhlagh and E. Magesan, Mitigating off-resonant error in the cross-resonance gate, *Phys. Rev. A* **105**, 012602 (2022).
- [52] A. Noguchi, A. Osada, S. Masuda, S. Kono, K. Heya, S. P. Wolski, H. Takahashi, T. Sugiyama, D. Lachance-Quirion, and Y. Nakamura, Fast parametric two-qubit gates with suppressed residual interaction using the second-order non-linearity of a cubic transmon, *Phys. Rev. A* **102**, 062408 (2020).
- [53] H. Xiong, Q. Ficheux, A. Somoroff, L. B. Nguyen, E. Dogan, D. Rosenstock, C. Wang, K. N. Nesterov, M. G. Vavilov, and V. E. Manucharyan, Arbitrary controlled-phase gate on fluxonium qubits using differential ac Stark shifts, *Phys. Rev. Res.* **4**, 023040 (2022).
- [54] Z. Ni, S. Li, L. Zhang, J. Chu, J. Niu, T. Yan, X. Deng, L. Hu, J. Li, Y. Zhong, S. Liu, F. Yan, Y. Xu, and Dapeng Yu, Scalable Method for Eliminating Residual ZZ Interaction between Superconducting Qubits, *Phys. Rev. Lett.* **129**, 040502 (2022).
- [55] P. Zhao, T. Ma, Y. Jin, and H. Yu, Combating fluctuations in relaxation times of fixed-frequency transmon qubits with microwave-dressed states, *Phys. Rev. A* **105**, 062605 (2022).
- [56] Z. T. Wang, P. Zhao, Z. H. Yang, Ye Tian, H. F. Yu, and S. P. Zhao, Escaping detrimental interactions with microwave-dressed transmon qubits, *Chin. Phys. Lett.* **40**, 070304 (2023).
- [57] A. Galiatdinov, A. N. Korotkov, and J. M. Martinis, Resonator-zero-qubit architecture for superconducting qubits, *Phys. Rev. A* **85**, 042321 (2012).
- [58] F. Yan, P. Krantz, Y. Sung, M. Kjaergaard, D. L. Campbell, T. P. Orlando, S. Gustavsson, and W. D. Oliver, Tunable coupling scheme for implementing high-fidelity two-qubit gates, *Phys. Rev. Appl.* **10**, 054062 (2018).
- [59] Y. Yanay, J. Braumüller, T. P. Orlando, S. Gustavsson, C. Tahan, and W. D. Oliver, Mediated interactions beyond the nearest neighbor in an array of superconducting qubits, *Phys. Rev. Appl.* **17**, 034060 (2022).
- [60] P. Zhao, K. Linghu, Z. Li, P. Xu, R. Wang, G. Xue, Y. Jin, and H. Yu, Quantum Crosstalk Analysis for Simultaneous Gate Operations on Superconducting Qubits, *PRX Quantum* **3**, 020301 (2022).
- [61] R. Barends *et al.*, Superconducting quantum circuits at the surface code threshold for fault tolerance, *Nature* **508**, 500 (2014).
- [62] L. H. Pedersen, N. M. Møller, and K. Mølmer, Fidelity of quantum operations, *Phys. Lett. A* **367**, 47 (2007).

- [63] F. Motzoi, J. M. Gambetta, P. Rebentrost, and F. K. Wilhelm, Simple Pulses for Elimination of Leakage in Weakly Nonlinear Qubits, *Phys. Rev. Lett.* **103**, 110501 (2009).
- [64] J. M. Gambetta, F. Motzoi, S. T. Merkel, and F. K. Wilhelm, Analytic control methods for high-fidelity unitary operations in a weakly nonlinear oscillator, *Phys. Rev. A* **83**, 012308 (2011).
- [65] B. Li, T. Calarco, and F. Motzoi, Suppression of coherent errors in cross-resonance gates via recursive DRAG, [arXiv:2303.01427](https://arxiv.org/abs/2303.01427).
- [66] G. J. Norris, L. Michaud, D. Pahl, M. Kerschbaum, C. Eichler, J.-C. Besse, and A. Wallraff, Improved parameter targeting in 3D-integrated superconducting circuits through a polymer spacer process, [arXiv:2307.00046](https://arxiv.org/abs/2307.00046).
- [67] C. J. Wood and J. M. Gambetta, Quantification and characterization of leakage errors, *Phys. Rev. A* **97**, 032306 (2018).
- [68] S.-I. Chu and D. A. Telnov, Beyond the Floquet theorem: Generalized Floquet formalisms and quasienergy methods for atomic and molecular multiphoton processes in intense laser fields, *Phys. Rep.* **390**, 1 (2004).
- [69] Y. Zhang, B. J. Lester, Y. Y. Gao, L. Jiang, R. J. Schoelkopf, and S. M. Girvin, Engineering bilinear mode coupling in circuit QED: Theory and experiment, *Phys. Rev. A* **99**, 012314 (2019).
- [70] A. Gandon, C. L. Calonnec, R. Shillito, A. Petrescu, and A. Blais, Engineering, control, and longitudinal read-out of floquet qubits, *Phys. Rev. Appl.* **17**, 064006 (2022).
- [71] A. Schneider, J. Braumüller, L. Guo, P. Stehle, H. Rotzinger, M. Marthaler, A. V. Ustinov, and M. Weides, Local sensing with the multilevel ac Stark effect, *Phys. Rev. A* **97**, 062334 (2018).
- [72] P. Zhao, R. Wang, M.-J. Hu, T. Ma, P. Xu, Y. Jin, and H. Yu, Baseband control of superconducting qubits with shared microwave drives, *Phys. Rev. Appl.* **19**, 054050 (2023).
- [73] K. N. Nesterov, Q. Ficheux, V. E. Manucharyan, and M. G. Vavilov, Proposal for Entangling Gates on Fluxonium Qubits via a Two-Photon Transition, *PRX Quantum* **2**, 020345 (2021).
- [74] S. Poletto, J. M. Gambetta, S. T. Merkel, J. A. Smolin, J. M. Chow, A. D. Córcoles, G. A. Keefe, M. B. Rothwell, J. R. Rozen, D. W. Abraham, C. Rigetti, and M. Steffen, Entanglement of Two Superconducting Qubits in a Waveguide Cavity via Monochromatic Two-Photon Excitation, *Phys. Rev. Lett.* **109**, 240505 (2012).
- [75] E. Zhang *et al.*, High-fidelity superconducting quantum processors via laser-annealing of transmon qubits, *Sci. Adv.* **8**, eabi6690 (2022).